Trans Indian Inst Met (2014) 67(5):629–650
DOI 10.1007/s12666-014-0386-7

TECHNICAL PAPER

TP 2790

# Kinetic–Statistical Approach in a Detailed Study of the Mechanism of Thermal Decomposition of Zinc–Iron-Intermetallic Phase

**Bojan Janković · Srećko Stopić · Bernd Friedrich**

Received: 2 August 2013 / Accepted: 2 January 2014 / Published online: 29 March 2014
© Indian Institute of Metals 2014

**Abstract** Kinetic–statistical approach was applied to investigate the mechanism of thermal decomposition of Zinc–Iron-intermetallic phase, as by product from neutral leach residues. In present paper, in order to characterize the tested material, the following experimental techniques were used: Rietveld analysis, scanning electron micrograph and tube furnace sample heating procedure. Based on dependence of Avrami constant in function of effective activation energy, it was found that at $T > 950$ °C, the process of crystal growth takes place in autocatalytic stage, under the conditions, where rate of nucleation rapidly increases. It was established that high nucleation rate can be attributed to formation of both Zn and Fe rich regions which provide a high number of heterogeneous nucleation sites. It has been proposed that emergence of line defects under ZnO branched crystals can serve as pin-points for secondary nucleation to occur. It was confirmed that increase in temperature in Zn vapor did not result in a decrease of existing in Zn constitutional vacancies.

**Keywords** Avrami exponent · Crystallization and kinetic models · Crystal growth · Intermetallic compound · Kinetics · Thermal decomposition

B. Janković (✉)
Faculty of Physical Chemistry, Department of the Dynamics and Structure of Matter, University of Belgrade, Studentski trg 12-16, P. O. Box 137, 11001 Belgrade, Serbia
e-mail: bojanjan@ffh.bg.ac.rs

S. Stopić · B. Friedrich
IME Process Metallurgy and Metal Recycling, RWTH Aachen University, Aachen, Germany

## 1 Introduction

Zinc is an important element especially for the steel industry and the formation of electric arc furnace dust (EAFD) leads to strong recycling activities. Zinc in primary fluidized bed calcine as well as in EAFD exists besides as simple oxides in a spinel form called zinc ferrite $ZnO{\cdot}Fe_2O_3$. A lot of studies have been conducted to find the most efficient way of zinc and iron recovery from the EAFD material due to environmental, technical and economical needs. Because of that there is a necessity for treatment of wastes containing zinc ferrites [1, 2]. Different hydrometallurgical ways for recovering zinc from ferrite-phases exist such as acidic or caustic leaching, microwave assisted extraction, EZINEX process, etc. [3–5].

Leaching with sulphuric acid to obtain high recovery yield is feasible based on the following reaction:

$$ZnFe_2O_4 + 4H_2SO_{4(aq)} \rightarrow ZnSO_{4(aq)} + Fe_2(SO_4)_3 + 4H_2O \quad (1)$$

Equation (1) can be expected even at room temperature, but the reaction rate is too slow. At elevated temperatures and longer leaching time, significant extraction yields >80 % will occur, but the process is unselective decreased [6]. Zinc extraction becomes even higher if the solid/acid ratio is lowered. During this process, calcium sulphate precipitates resulting from low concentration of sulphuric acid and it remains until end of process. Because of unselective leaching a yield of zinc is decreased [6]:

$$ZnFe_2O_4 + 2[OH^-] \rightarrow ZnO_2^{2-} + Fe_2O_3 + H_2O. \quad (2)$$

Other researches [5] have studied leaching kinetics of zinc ferrite in aqueous hydrochloric acid solutions

according to the reaction (3) and found that it is possible to precipitate ferric chloride, in the pH range of 3–4 and using air mixing:

$$ZnFe_2O_4 + 2HCl \rightarrow ZnCl_2 + Fe_2O_3 + H_2O \quad (3)$$

Their experiments have reached up to 90 % zinc recovery under pH values between of 3–4 at 90 °C. Unsuccessful experiments on ammonia leaching were conducted, where the EAF dust was firstly washed to solubilize the zinc oxide and then leached with ammonium chloride. But the zinc ferrite remains in residue. An organic acid process was also able to recover zinc from ferrite, when additional leaching step was introduced [5].

Today's commercial operations reach almost complete winning of zinc from zinc ferrite are mostly based on fuming operations that reduces ferrite and vaporizes zinc. Such pyrometallurgical applications use a reduction media such as carbon monoxide, hydrogen or coke [7].

The carbothermic method [8] requires a minimum temperature of 800 °C and the partial pressure of zinc vapor which remains below $p = 0.014$ bars. A full reduction of EAF dust with hydrogen at lower temperatures produces both iron and zinc with double hydrogen requirement, compared to the selective reduction that only produces zinc [2]. The worldwide standard is thermal reductive treatment in a Waelz process [9] enabling strong destruction of the zinc ferrite whereby producing a slag with very limited probability for use and high energy input.

In this work an alternative approach to the thermal decomposition process of the spinel phase has been investigated avoiding low kinetics as well as unselective, slow, and costly reduction. It is the consequent follow up of the monitor researching of Püllenberg [10] which has already investigated the neutral leaching of thermally decomposed iron–zinc concentrate at weak reductive atmospheres (up to 10 % of CO).

In this paper, we present a completely new theoretical concept to explain the detailed mechanism of the isothermal decomposition of Zinc–Iron-intermetallic phase (ferrite), as by-product from neutral leach residues, which, in itself, is a very complex physico-chemical process. The procedure contains the kinetic–statistical approach. The kinetic display is based on the explanation of the process from the standpoint of the theory of the nucleation and growth of a new phase [11–14]. The statistical display is based on the application of the Weibull probability model [15–17], through the introduction of the specific distribution functions that can describe the behavior of the system that has some degree of variability. This model has an interesting potential for describing the decomposition kinetics of the considered system, when the system is subjected to the elevated temperatures under controlled experimental conditions (the "failure" of the system after a given time subjected to the operating temperature stress conditions).

## 2 Experimental

### 2.1 Material Characterization

The zinc contained leach residue was obtained from former company Ruhr-Zink, Datteln, Germany, with a moisture content of 23 %. Before the experimental investigation, the sample was dried at 120 °C overnight in order to eliminate the moisture presence. The Rietveld X-ray diffraction (XRD) analysis of an initial sample has shown the following chemical composition [in %]: 40.9 $ZnFe_2O_4$, 16.5 $CaSO_4$, 6.4 $MgSO_4$, 13.6 $Zn_2SiO_4$, 11.3 $PbSO_4$, 4.4 $KFe_3(SO_4)_2(OH)_6$, and 6.9 related to the others compounds. This phase change made materials more soluble and suitable for the leaching process, which was reported in [1]. The gaseous phases of PbO and $SO_2$ were formed during thermal decomposition and removed with nitrogen as the carrier gas. At 1,150 °C, the chemical composition of the final decomposed material amounted [in %]: 57.0 $Fe_3O_4$, 28.9 $Ca_2ZnSi_2O_7$, 8.4 ZnO, 5.0 $Mg_2SiO_6$ and 0.7 $ZnAl_2O_4$. A scanning electron microscope (model ZEISS DSM 982 Gemini) (SEM) was used for the characterization of the obtained particles. The SEM images were used to study the surface morphology.

### 2.2 Isothermal Measurements

After 15 min of heating the samples in order to eliminate the contained moisture, these were used in the thermal treatment experiments performed in the tube furnace. At the fixed operating temperatures ($T = 600$, 750, 950, 1,150 °C), the four experiments were performed at each operating temperature in the certain time intervals (15, 20, 25, 30, 35, 40, 45, 50, 55 and 60 min). The experiments were repeated three times. After reaching the aimed temperature, 1 g of the zinc contained leach residue was inserted in a tubular furnace, under a constant nitrogen gas, with a flow rate of $\varphi = 1$ L min$^{-1}$. After beginning of the thermal treatment of dried sample at the fixed operating temperature, the reaction time was measured by chronometer (in digits form). After that, the specimen was taken out from the furnace and placed in the exsiccator. The weight results were noted as an average mass lost of the specimen, in order to calculate the decomposition rate.

The conversion fraction ($\alpha$) in the isothermal measurement at the considered operating temperature $T$ is calculated by the following equation:

$$\alpha = \frac{m_{o(15)} - m_t}{m_{o(15)} - m_f} \tag{4}$$

where $m_{o(15)}$ is the initial mass of the sample [for time at $t = 15$ min, after removing of any remaining moisture at a given temperature (the time period from $t = 0$ min to $t = 15$ min at each of the considered operating temperature $T$, corresponds to time scale where the removal was done for the possible residual moisture)], $m_t$ is the mass of the sample at time $t$, and $m_f$ is the final constant mass of the sample, after the establishment of the saturation (the saturation involves reaching the conversion value of $\alpha = 1.00$). Thus, the conversion data are calculated for completely dry samples at each of the observed temperatures. The decomposition of zinc contained leach residue in an inert atmosphere at every considered operating temperature begins after the fifteenth minute.

## 3 Theoretical Background

### 3.1 Phase Transformation Kinetics

Most solid state transformations do not occur instantaneously because obstacles impede the course of the reaction and make it dependent on time. For example, since most transformations involve the formation of at least one new phase that has a composition and/or crystal structure different from that of the parent, some atomic rearrangements via diffusion are required. A second impediment to the formation of a new phase is the increase in energy associated with the phase boundaries that are created between parent and product phases. From a micro-structural standpoint, the first process to accompany a phase transformation is nucleation—the formation of very small (often submicroscopic) particles, or nuclei, of the new phase, which are capable of growing. Favorable positions for the formation of these nuclei are imperfection sites, especially grain boundaries. The second stage is growth, in which the nuclei increase in size. During this process, some volume of the parent phase disappears. The transformation reaches completion if growth of these new phase particles is allowed to proceed until the equilibrium fraction is attained.

As would be expected, the time dependence of the transformation rate (which is often termed the kinetics of a transformation) is an important consideration in the heat treatment of materials. With many kinetic investigations, the fraction of reaction that has occurred is measured as a function of time, while the temperature is maintained constant. Data are plotted as the fraction of transformed material ($\alpha$) versus the time ($t$) (the kinetic conversion curves). The obtained curves represent the typical kinetic behavior for most solid-state reactions. For special cases of nucleation and growth, it is possible to derive the well-known analytical description of transformation kinetics according to Johnson–Mehl and Avrami (JMA) [11–14]. For solid-state transformations displaying the kinetic behavior through $\alpha$–$t$ curves, the fraction of transformation ($\alpha$) is a function of time ($t$) as follows:

$$\alpha = 1 - \exp[-(K_A t)^n], \ \alpha \in [0, 1] \tag{5}$$

where $K_A$ and $n$ represent the Avrami rate constant, and the Avrami constant (or JMA exponent), respectively. Equation (5) is often referred to as the Avrami equation [12–14]. Usually, the Avrami rate constant $K_A$ is written in the form of the composite Avrami rate constant $k_A$ (i.e. $k_A = K_A^n$). It was shown that $k_A$ [the dimension of which is given in $(\text{time})^{-n}$] is not only a function of temperature, but also a function of the Avrami constant, $n$ [18]. As a result, use of $K_A$ should be more preferable than use of $k_A$, due to partly to the facts that it is independent of the Avrami constant $n$ and its dimension is given in $(\text{time})^{-1}$. It should be noted that both $k_A$ (and hence $K_A$) and $n$ are constants specific to a given crystalline morphology and type of nucleation for a particular crystallization condition [19] and that, based on the original assumptions of the theory, the value of the Avrami constant $n$ should be an integer, ranging from 1 to 4. The value of $K_A$ and $n$ can be obtained from the linear relationship as $\ln[-\ln(1 - \alpha)] = n\ln K_A + n\ln t$ [12–14]. By plotting $\ln[-\ln(1-\alpha)]$ against $\ln t$ for different operating temperatures, the JMA plots can be evaluated, in the case of $\alpha$ range ($\Delta\alpha$) where there is a linearity of the data used.

The Avrami rate constant ($K_A$) can be presented in the form of the Arrhenius equation as:

$$K_A = k_A^{\frac{1}{n}} = k_o \cdot \exp\left(-\frac{E_a}{RT}\right) \tag{6}$$

where $k_o$ represents the pre-exponential factor [$\text{time}^{-1}$], $E_a$ is the *apparent* or the *effective* activation energy [J $\text{mol}^{-1}$], $R$ is the gas constant [J $\text{K}^{-1}$ $\text{mol}^{-1}$], and $T$ is the absolute temperature [K]. Temperature is one variable in a heat treatment process that is subject to control, and it may have a profound influence on the kinetics and thus on the rate of the transformation. For most solid state reactions, and over specific temperature ranges, the rate increases with temperature according to the Eq. (6). Processes that exhibit the temperature dependence of the rates through the relationship presented by Eq. (6) are sometimes termed as the thermally *activated*. The rate of the process expressed through Eq. (5), can be obtained by differentiating Eq. (5) in respect to time ($t$) and after rearranging of some terms, we can finally get the expression of the form:

$$\frac{d\alpha}{dt} = K_A \cdot f(\alpha) = K_A \cdot n(1-\alpha)[-\ln(1-\alpha)]^{\frac{(n-1)}{n}} \equiv k_A^{\frac{1}{n}} \cdot n(1-\alpha)[-\ln(1-\alpha)]^{\frac{(n-1)}{n}} \quad (7)$$

where $f(\alpha)$ is the differential form of the function of reaction mechanism. The rate of the process expressed by the differential kinetic equation [Eq. (7)] can be rearranged and integrated as:

$$\int_0^{\alpha} \frac{d\alpha}{f(\alpha)} \equiv g(\alpha) = [-\ln(1-\alpha)]^{\frac{1}{n}} = K_A \cdot t = k_A^{\frac{1}{n}} \cdot t. \quad (8)$$

In Eq. (8), $g(\alpha)$ is the integral form of the function of reaction mechanism. By plotting linearly $g(\alpha)$ for several conversion grade $\alpha$ observed experimentally, it is possible to obtain $K_A$ for each operating temperature, which represents the slope of the linear adjustment of $g(\alpha)$ against time ($t$). The plot of calculated $\ln K_A$ [$\equiv (1/n)\cdot\ln k_A$] against $1/T$ according to the Arrhenius postulate (as $\ln K_A = (1/n)\cdot\ln k_A = \ln(k_o) - E_a/RT$) allow to deduce the apparent activation energy ($E_a$) and the pre-exponential factor ($k_o$).

In the case of continuous nucleation, the *nucleation rate* function $I(t)$ (for quantifying nucleation rate $I$ as a function of time throughout the course of crystallization) can be introduced as [20]:

$$I(t) = I_c(1+m)t^m, \quad (9)$$

where $I_c$ is the nucleation rate constant (a temperature-dependent, but time-independent parameter, the dimension of which is given in (number of nuclei/[$s^{m+1}$ $cm^3$)], and $m$ represents the *nucleation index*. In the considered case, the Avrami constant can be presented in a more specific mathematical definition as:

$$n = d + m + 1 \quad (9a)$$

where $d$ represents the geometric or *dimensionality index* (e.g. $d = 1$ for rod, $d = 2$ for disc, and $d = 3$ for sphere). According to Eq. (9a), the traditional sense of the Avrami constant $n$ in describing the dimensionality of the crystal geometry is restored with the geometric or dimensionality index $d$, but, more importantly, abnormality in the experimental observation of the Avrami constant $n$ (viz. fractional values of $n$, or the values of $n$ greater than four) can now be theoretically explainable by the introduction of the *nucleation index* $m$. The qualitative description of the *nucleation index m* (for a fixed value of the geometric index $d$) in describing the nucleation mechanism throughout the course of the crystallization process can be described in a few significant items: (*i*) $m = -1$: *Nucleation mechanism*: Instantaneous; *Nature of the nucleation rate over crystallization time*: Constant, (*ii*) $-1 < m < 0$: *Nucleation mechanism*: Instantaneous and sporadic; *Nature of the nucleation rate over crystallization time*: Gradually decreasing with time and approaching a constant value at a certain time, (*iii*) $m = 0$: *Nucleation mechanism*: Sporadic; *Nature of the nucleation rate over crystallization time*: Steadily increasing with time, (*iv*) $0 < m < 1$: *Nucleation mechanism*: Sporadic; *Nature of the nucleation rate over crystallization time*: Increasing with time, (*v*) $m > 1$: *Nucleation mechanism*: Sporadic; *Nature of the nucleation rate over crystallization time*: Increasing strongly with time.

Strictly speaking, the JMA kinetic parameters ($n$, $k_o$ and $E_a$) can only have certain values, pertaining to specific growth and nucleation models [21]. Mixtures of the specific nucleation models are not considered in the original derivation of JMA kinetics. However, it can be proven (by numerical procedure) for such mixtures of nucleation models that, although the JMA description does not hold exactly, a very good approximation to the observed kinetics can still be given by the JMA description according to Eqs. (5) and (6) [21]. Thus, also intermediate values of the JMA kinetic parameters then are possible [21]. Determined values for the *effective* kinetic parameters can then be interpreted in terms of the basic nucleation and growth models, recognizing the interdependence of the JMA kinetic parameters. It has been shown that the *apparent* (*effective*) activation energy is given by the following weighted average of the *activation energies* of the involved nucleation and growth processes as [21]:

$$E_a = \frac{(n-1)E_G + E_N}{n} = \frac{(d+m)E_G + E_N}{(d+m+1)} \quad (10)$$

where $E_G$ and $E_N$ represent the activation energies for the growth and nucleation. If $E_a$ can be measured as function of $n$ (by variation of the nucleation index through the numerical procedure), in that case Eq. (10) allows us to determine the corresponding values of $E_G$ and $E_N$, separately.

The apparent (*effective*) activation energy values ($E_a$) can be calculated at the different and constant values of conversion fraction (or the fraction of transformation) ($\alpha$), combining Eqs. (6) and (8), and presenting them in logarithmic form, so that we get [22]:

$$-\ln t_{\alpha_{k,i}} = \ln\left[\frac{(k_o)_{\alpha_{k,i}}}{g(\alpha_{k,i})}\right] - \frac{E_{a,\alpha_{k,i}}}{RT_i}. \quad (11)$$

Using data at which in different operating temperature runs ($T_i$) the same value $\alpha = \alpha_{k,i} = const.$ was reached, the linear relationship $-\ln t_{\alpha k,i}$ versus $1/T_i$ with a slope proportional to $E_{a,\alpha k,i}$ could be established. This method provides a check of invariance of $E_a$ with respect to conversion fraction, $\alpha$.

The local Avrami constant ($n_{loc}$) is employed to have the derivative of the Avrami plot against the fraction of transformation, which efficiently gives the local value of $n$ with $\alpha$ [23]. The local Avrami constant is deduced by:

$$n_{loc} \equiv n(\alpha) = \frac{\partial \ln\left\{\ln\left[\frac{1}{(1-\alpha)}\right]\right\}}{\partial \ln(t)}. \quad (12)$$

The value of local Avrami constant [$n(\alpha)$] gives information about the nucleation and growth behavior, when the crystallized volume fraction is $\alpha$.

Once the generalized Avrami constant is known (as described above), we can then calculate the Avrami rate constant $K_A$ from half-time analysis [24]. The half-time ($t_{0.50}$) is defined as the time required to achieving 50 % of the maximum conversion during the isothermal experiment [24]. The Avrami rate constant ($K_A$) can be calculated directly from the reciprocal half-time ($t_{0.50}^{-1}$) according to the following equation [25]:

$$K_A = (\ln 2)^{\frac{1}{n}} \cdot t_{0.50}^{-1}. \quad (13)$$

For the mechanism in which the Avrami constant $n > 1.00$, the rate approaches zero at the beginning of the process (i.e. $t \to 0$), and when the process nears completion (i.e. $t \to \infty$). The maximum rate of the isothermal transformation occurs at time $t_{max}$, which corresponds to the inflection point of the $\alpha$ versus $t$ curve, where the second derivative of $\alpha(t;T)$ vanishes. Therefore, the $t_{max}$ can be calculated from the following equation [24, 26]:

$$t_{\max} = \left[\frac{(n-1)}{nk_A}\right]^{\frac{1}{n}}. \quad (14)$$

Since the half-time measurements provide a route to calculate $K_A$ (as well as the composite Avrami rate constant, $k_A$), the relation that connects $t_{max}$ and $t_{0.50}$ can be expressed in the form [24]:

$$t_{\max} = \left[\frac{(n-1)}{n\ln 2}\right]^{\frac{1}{n}} \cdot t_{0.50}. \quad (15)$$

The ratio $t_{max}/t_{0.50}$ allows us to compare the differences between $t_{0.50}$ and $t_{max}$ if they exist, for a given value of the Avrami constant ($n$), evaluated at the considered operating temperature.

One of the frequently applied tests to verify the applicability of the JMA mechanism is based on the properties of two special functions, which are labeled as $Y(\alpha)$ and $Z(\alpha)$ functions [27, 28]. In isothermal conditions, however, the magnitude $K_A$ [expressed through Eq. (6)] in Eq. (7) is constant and the rate of the process ($d\alpha/dt$) is approximately equal to $f(\alpha)$ function, as:

$$Y(\alpha) = \left(\frac{d\alpha}{dt}\right) \approx f(\alpha) \quad (16)$$

If the rate of the process at considered operating temperature is plotted as a function of $\alpha$ its shape corresponds to the $f(\alpha)$ function. It is convenient to normalize the $Y(\alpha)$ plot within [0,1] interval. Combining Eqs. (7) and (8), the other function $Z(\alpha)$ can be defined as:

$$Z(\alpha) = \left(\frac{d\alpha}{dt}\right) \cdot t = f(\alpha) \cdot g(\alpha) \quad (17)$$

For practical reasons this function is normalized within [0,1] interval. The $Y(\alpha)$ and $Z(\alpha)$ functions exhibit maxima at $\alpha_m$ and $\alpha_p^{\infty}$, respectively. The maximum of the $Y(\alpha)$ function for the JMA mechanism depends on the value of the Avrami constant:

$$\alpha_m = 1 - \exp\left[\frac{(1-n)}{n}\right], \text{ for } n > 1.00;\ \alpha_m = 0, \text{ for } n \le 1.00. \quad (18)$$

The value of $\alpha_m$ is always lower than the maximum of the $Z(\alpha)$ function, $\alpha_p^{\infty}$. The latter is a constant in the case of the JMA mechanism, and amounts $\alpha_p^{\infty} = 0.632$.

This procedure can be used as the simple test of the applicability of JMA theory of nucleation and growth kinetics, in the case of the investigated decomposition process. On the other hand, if the $Y(\alpha)$ function has a maximum in the interval between 0 and $\alpha_p$ (where $\alpha_p$ represents the conversion fraction, which corresponds to the maximum value of differential rate conversion curves, presented as $d\alpha/dt$ versus $t$), i.e. for $n > 1.00$, then the Avrami constant ($n$) can be calculated from Eq. (18), but now re-written in a somewhat different mathematical form, as $n = 1/[1 + \ln(1-\alpha_m)]$.

### 3.2 The Weibull Probability Model

From the basic properties of Weibull standard probability model [15–17], we can infer that the Weibull distribution represents the specific distribution that can describes the behavior of systems (or events) that have some "*degree of variability*". The term "*degree of variability*" in the case of chemical systems, would apply to such reaction systems which provide real structural variations of the chemical entities during exposure to the thermal stress conditions, under various heating programs. This model has an interesting potential for describing the decomposition kinetics of the investigated system, when the system is subjected to heating in a controlled temperature gradient (the failure of the system after a given time subjected to the temperature stress conditions).

In isothermal experimental conditions, if the sample is heated up to the desired operating temperature ($T$), the fraction of transformation ($\alpha$) can be considered as the probability of the realization of decomposition process of

interest [$F(t)$] at the particular operating temperature $T_l$ ($l = 1,2,\ldots,p$), so this probability under the isothermal schedule takes the form of the two-parameter Weibull distribution function [15, 16], as:

$$F(t) \equiv \alpha(t) = 1 - \exp\left[-\left(\frac{t}{\eta}\right)^{\beta}\right], \tag{19}$$

where $t$ is the time and represents the random variable, for $T = \text{const.}$, $\eta$ is the scale parameter (a change in $\eta$ parameter, has the same effect of stretching out the probability function; the larger the scale parameter, the more spread out the distribution), $\beta$ is the shape parameter (different values of $\beta$ can have marked effects on the behavior of the distribution and determines its shape). Equation (19) represents the standard Weibull probability model, according to classification by Murthy et al. [17]. Based on the known characteristics [17], the Weibull distribution should be a very versatile and desirable model, which easily fits many experimental data sets requiring a sigmoid shape. If we have a kinetic curve that is symmetrical on each side of the inflection point, then in that case, the Weibull distribution is not acceptable for modeling situations.

If we compare the Eqs. (5) (Avrami equation) and (19), we can confirm the validity of the following equalities between the JMA model parameters and the parameters of the standard Weibull model:

$$n = \beta \tag{20}$$

and

$$K_A = \eta^{-\frac{1}{\beta}} \Rightarrow k_A = \frac{1}{\eta}, \tag{21}$$

which implies that the Avrami constant ($n$) is equal to the shape parameter ($\beta$), and the composite Avrami rate constant $k_A$ is equal to the reciprocal value of the scale parameter ($k_A = \eta^{-1}$).

Differentiating Eq. (19) by time ($t$), we can obtain the corresponding *rate function* [*pdf* probability density function (the rate of process at $T = \text{const.}$)] in isothermal conditions, as:

$$\frac{d\alpha(t)}{dt} = \frac{\beta}{\eta}\left(\frac{t}{\eta}\right)^{\beta-1} \cdot \exp\left[-\left(\frac{t}{\eta}\right)^{\beta}\right] \tag{22}$$

Comparing Eq. (22) with Eq. (7), we have the following correlations:

$$K_A^n \equiv K_A^{\beta} = \left(\eta^{-\frac{1}{\beta}}\right)^{\beta} = \eta^{-1} (\text{with } n \equiv \beta), \tag{23}$$

$$(1 - \alpha) = 1 - F(t) \equiv \exp\left[-\left(\frac{t}{\eta}\right)^{\beta}\right] = S(t), \tag{24}$$

where the remaining fraction of decomposed material [$(1-\alpha)$] corresponds to the *survival* function [$S(t)$] of the two-parameter Weibull distribution in isothermal conditions, which gives the probability that given process still exists at duration $t$, or more generally, the probability that the process of interest has not occured by duration $t$. The survival function is often used in failure time analysis [29, 30]. One the use of the survival function is to predict quantiles of the survival time. For example, the median survival time [designated by $t_{50}$, which corresponds to the half-time ($t_{0.50}$)] may be of interest (the median may be preferable to the mean as a measure of centrality if the data are highly skewed), so that we can calculate $t_{50}$ as the solution to $S(t) = 1–0.50 = 0.50$ (expressed in %). Likewise, the time by which 90 % of investigated material will have failed ($t_{90}$) is given by the solution to $S(t) = 1–0.90 = 0.10$.

The third term of the right-hand side of Eq. (7) corresponds to the following term in the *rate function* equation:

$$[-\ln(1-\alpha)]^{\frac{(n-1)}{n}} \equiv \left[\left(\frac{t}{\eta}\right)^{\beta}\right]^{\frac{(\beta-1)}{\beta}} = \left(\frac{t}{\eta}\right)^{\beta-1} \tag{25}$$

The term $(\beta/\eta)\cdot(t/\eta)^{\beta-1}$ [Eqs. (22), (23) and (25)] represents the *hazard* function $H(t)$ [31]. The connection between the hazard and survival functions is given by following equation:

$$H(t) = \frac{(d\alpha(t)/dt)}{S(t)} = \frac{(d\alpha(t)/dt)}{1 - F(t)} = -\frac{\partial}{\partial t}\ln[1 - F(t)] = -\frac{\partial}{\partial t}\ln[S(t)]. \tag{26}$$

Therefore,

$$S(t) = \exp[-H^*(t)], \tag{27}$$

where

$$H^*(t) = \int_0^t H(t)dt. \tag{28}$$

The function $H^*(t)$ is called the *cumulative* hazard function or the *integrated* hazard function.

The Weibull probability plots (WPP) allow us to calculate the distribution parameters $\beta$ and $\eta$ [32]. Taking logarithms twice of both sides of each of the two-parameter Weibull distribution function in Eq. (19) yields:

$$\ln[-\ln(1 - F(t))] = \beta \ln\left(\frac{1}{\eta}\right) + \beta \ln t. \tag{29}$$

Let $Y = \ln[-\ln(1-F(t))]$ and $X = \ln t$. Then we have $Y = \beta\ln(1/\eta) + \beta X$. The plot is now on a linear scale. From the slope of obtained straight line, the shape parameter ($\beta$) can be calculated. Then, from intercept,

and for known value of $\beta$, we can calculate the value of the scale parameter ($\eta$), at $T = const$.

### 3.2.1 Reactivity Distribution

Reactivity distributions for the complex systems are often characterized by distribution of the apparent activation energies. The characteristic of a reactivity distribution is that the *reaction profile* [33] is broader than that of a first-order reaction derived from the shift of any measure of constant conversion *versus* time/temperature or the heating rate [34]. A diagnostic of inappropriate kinetic analysis common in the published literature is that the low apparent activation energy will be derived from a single thermo-analytical (TA) experiment having a broad reaction profile. However, the Weibull distribution is one of three apparent activation energy distribution models [34, 35] which has been identified that could overcome this problem. In the case of nucleation and growth model, the fraction decomposed can be expressed by the reactivity distribution in the following form:

$$\alpha = 1 - \int_0^{\infty} \left\{ \exp\left[ -\left[ k_o \cdot \exp\left( -\frac{E_a}{RT} \right) \right]^{\beta} \right] \cdot t^{\beta} \right\} \times f(E_a) dE_a \ (\text{for } n = \beta), \tag{30}$$

where $f(E_a)$ represents the density distribution function of the apparent activation energies ($E_a$), where standardization condition is valid, and can be expressed in the form [36]:

$$\int_0^{\infty} f(E_a) dE_a = 1. \tag{31a}$$

The function $f(E_a)$ is the two-parameter density Weibull distribution function, which is given in the form:

$$f(E_a) = \frac{\beta_{E_a}}{\eta_{E_a}} \left( \frac{E_a}{\eta_{E_a}} \right)^{\beta_{E_a}-1} \cdot \exp\left[ -\left( \frac{E_a}{\eta_{E_a}} \right)^{\beta_{E_a}} \right], \tag{32}$$

where $\beta_{E_a}$ [dimensionless] and $\eta_{E_a}$ [kJ mol$^{-1}$] represent the shape and scale (*width*) distribution parameters, correlated to the apparent (*effective*) activation energy ($E_a$), as the random variable.

The mean apparent activation energy ($\mu \equiv E_{ao}$) (*first moment*) can be defined by [34]:

$$\mu \equiv E_{ao} = \eta_{E_a} \cdot \Gamma\left( \frac{1}{\beta_{E_a}} + 1 \right), \tag{33}$$

where $\Gamma(\cdot)$ is the Gamma function and adequate equation in Abramowitz and Stegun Mathematical handbook [37] was used to evaluate Gamma function as a function of $\beta_{E_a}$.

The values of distribution parameters, $\beta_{E_a}$ and $\eta_{E_a}$ can be found from conversion-dependency of the apparent (*effective*) activation energy in the form of two-parameter Weibull probability function:

$$\alpha(E_a) \equiv F(E_a) = 1 - \exp\left[ -\left( \frac{E_a}{\eta_{E_a}} \right)^{\beta_{E_a}} \right], \tag{34}$$

and taking logarithms twice of both sides of each of the probability function in Eq. (34) we have:

$$\ln[-\ln(1 - \alpha(E_a))] = \beta_{E_a} \cdot \ln\left( \frac{1}{\eta_{E_a}} \right) + \beta_{E_a} \cdot \ln E_a \tag{35}$$

Scale parameter ($\eta_{E_a}$) and shape parameter ($\beta_{E_a}$) can be calculated from the *intercept* ($\equiv \beta_{E_a} \cdot \ln(1/\eta_{E_a})$) and the *slope* ($\equiv \beta_{E_a}$) of the obtained straight line. Based on calculated values of the parameters $\beta_{E_a}$ and $\eta_{E_a}$, the corresponding reactivity distribution for investigated process can be evaluated.

## 4 Results and Discussions

### 4.1 Analysis of Experimentally Obtained Integral and Differential Kinetic Curves

The experimentally obtained isothermal conversion ($\alpha$–$t$) curves for the decomposition process of Zinc–Iron-intermetallic phase ("iron–zinc concentrate"), at the operating temperatures of 600 °C, 750 °C, 950 °C and 1,150 °C in an inert atmosphere are presented in Fig. 1.

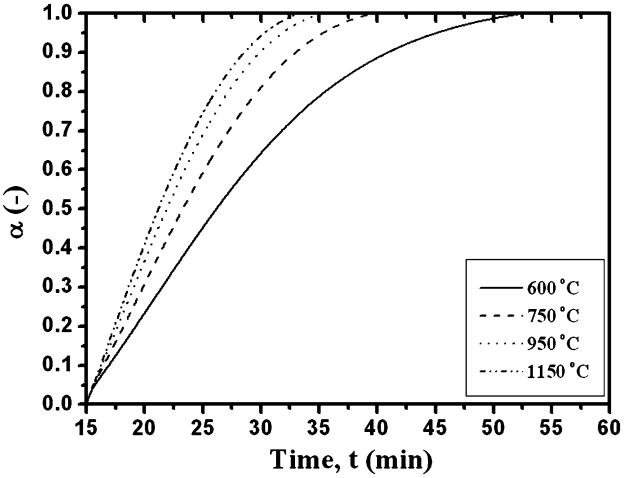


**Fig. 1** The experimentally obtained conversion ($\alpha$–$t$) curves for Zinc–Iron-intermetallic phase decomposition process, at the different operating temperatures (600 °C, 750 °C, 950 °C and 1,150 °C) in an inert atmosphere (*curves* are presented in B-*spline* graphic configurations)

The rate of decomposition increases with an increase in operating temperature, and at $T = 1{,}150$ °C, approximately 100 % of considered transformation is achieved in less than 35 min. In that case, the decomposition process in an inert atmosphere should be performed at the operating temperatures of $T \geq 600$ °C to investigate the whole decomposition process, within a reasonable reaction time period.

The experimental differential conversion ($d\alpha/dt$–$t$) curves obtained at the different operating temperatures (600 °C, 750 °C, 950 °C and 1,150 °C) for the investigated decomposition process are shown in Fig. 2.

Figure 2 shows that all $d\alpha/dt$ versus $t$ curves exhibit the maximum decomposition rate ($(d\alpha/dt)_{max}$) at value $t_{max} > 0$. The increase in operating temperature leads to a narrowing of the reaction profiles on considered curves (Fig. 2). Table 1 shows the values of $(d\alpha/dt)_{max}$, $(d\alpha/dt)_{max}/2$ (the rate corresponding to half the maximum value), $t'_{m/2}$ (the time on the descent of the corresponding $d\alpha/dt$ versus $t$ curve) and $t_{max}$ [the time which corresponds to a value of $(d\alpha/dt)_{max}$] for the differential conversion curves in Fig. 2.

It can be seen from Table 1 that the values of $(d\alpha/dt)_{max}$ and $(d\alpha/dt)_{max}/2$ increase with increasing in operating temperature, while the values of $t^{*}_{m/2}$ and $t_{max}$ decrease with increasing of $T$ from 600 °C to 1,150 °C, which directly indicates the narrowing of the reaction profile. The presented rate-time features of differential conversion curves are useful for the basic classification of kinetic models. Thus, the above results are designated on the sigmoid group of kinetic (nucleation and growth) models, such as JMA (Johnson–Mehl–Avrami), SB (Šesták-Berggren), or PT (Prout-Tompkins) models (this group of models has $(d\alpha/dt) = (d\alpha/dt)_{max}$ at $t = t_{max} > 0$) [38]. For the mentioned models, the rate-time profiles show the characteristic bell-shaped

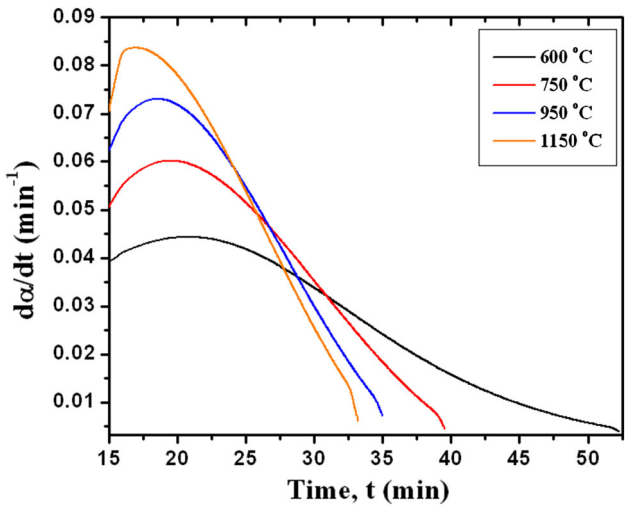


**Fig. 2** The experimentally obtained differential conversion ($d\alpha/dt$–$t$) curves for Zinc–Iron-intermetallic phase decomposition process, at the different operating temperatures (600 °C, 750 °C, 950 °C and 1,150 °C)

**Table 1** The rate-time characteristics $(d\alpha/dt)_{max}$, $(d\alpha/dt)_{max}/2$, $t'_{m/2}$ and $t_{max}$ for the differential conversion curves ($d\alpha/dt$–$t$) of the isothermal decomposition of zinc–iron-intermetallic phase, at the different operating temperatures (600 °C, 750 °C, 950 °C and 1,150 °C) (the differential conversion curves were derived on the basis of numerical differentiation of experimental $\alpha$–$t$ curves, so that during the formation of $d\alpha/dt$–$t$ curves, the errors which arise from the background noise were included)

| $T$ (°C) | $(d\alpha/dt)_{max}$ ($min^{-1}$) | $(d\alpha/dt)_{max}/2$ ($min^{-1}$) | $t'_{m/2}$ (min) | $t_{max}$ (min) |
|---|---|---|---|---|
| 600 | 0.04433 | 0.02217 | 36.595 | 20.909 |
| 750 | 0.06019 | 0.03009 | 31.470 | 19.545 |
| 950 | 0.07307 | 0.03654 | 28.683 | 18.636 |
| 1,150 | 0.08371 | 0.04186 | 27.167 | 16.818 |

feature, where the peak maximum is shifted to the shorter values of reaction time, with increasing values of the experimental parameter, such as the operating temperature, under isothermal conditions [38]. This behaviour manifests all $d\alpha/dt$–$t$ curves presented in Fig. 2. These properties are often present in complex processes that may have the reaction step/steps with an autocatalytic type of kinetic mechanism. However, it should be noted, that the above-mentioned results are only preliminary kinetic analysis. Therefore, this case requires further, a more detailed study.

### 4.2 Isoconversional Analysis

The fundamental assumption of the isothermal isoconversional methods is that a single rate equation is applicable only to a single extent of conversion and to the time region ($\Delta t$) related to this conversion. In other words, the isoconversional methods describe the kinetics of the process by using the multiple single rate (or single-step) kinetic equations, each of which is associated with a certain extent of conversion. With regard to this advantage, the isoconversional methods allow complex (i.e., multi-step) processes to be detected via a variation of the apparent (*effective*) activation energy ($E_a$) with a conversion, $\alpha$. Conversely, independence of $E_a$ on $\alpha$ is a sign of a single-step process. The apparent activation energy-conversion correlation, usually corresponds to the change of the reaction mechanisms; it may reflect relative contributions of the parallel reaction channels to the overall kinetics of the process.

Figure 3 shows the dependence of $E_a$ on $\alpha$ evaluated by application of Eq. (11), for the isothermal decomposition process of Zinc–Iron-intermetallic phase (ferrite), using the different operating temperatures.

As shown in Fig. 3, the dependence $E_a = E_a(\alpha)$ exhibits a progressive increase in $E_a$ values, in the whole range of the considered conversion ($\alpha$) values ($0.05 \leq \alpha \leq 0.95$).

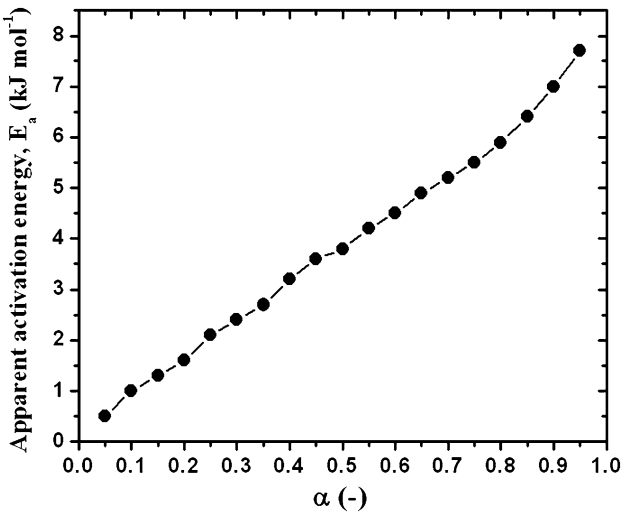


**Fig. 3** The dependence of the apparent activation energy ($E_a$) on the fraction of transformation (α), evaluated by application of Eq. (11), for Zinc–Iron-intermetallic phase decomposition process

This behaviour of $E_a$ values with α is the characteristic for the processes involving parallel competing reactions [39]. It can be seen from Fig. 3, that the apparent activation energy varies in the range of 0.5–7.7 kJ mol$^{-1}$, so that on the basis of the shape of $E_a-\alpha$ curve, we can conclude that the investigated decomposition process takes place through the parallel competing reactions, which have different contributions to the overall process [40]. If we assume that the decomposition process of such a complex system could take place through the model of nucleation and growth of new phases, the above illustrated variations of $E_a$ on α could indicate on the alternated behaviour of the Avrami constant ($n$), starting from the lower range of the operating temperatures ($\Delta T$ = 600–750 °C) to a higher range of the operating temperatures ($\Delta T$ = 950–1,150 °C). This behaviour of the Avrami constant can change the spatial dimensionality of the resulting products of investigated process.

### 4.3 Double Logarithmic ('Ln–Ln') Plot Analysis

The values of $K_A$ and $n$ were calculated from the linear relationship $\ln[-\ln(1-\alpha)]$ against $\ln t$ at the different operating temperatures (600 °C, 750 °C, 950 °C and 1,150 °C). The data for $0.15 \leq \Delta\alpha \leq 0.95$ are almost located on straight lines (not shown). The values of intercepts of the obtained straight lines ($n\ln K_A$), the logarithmic values of $K_A$ ($\ln K_A$), the values of $K_A$, as well as the values of the Avrami constant ($n$), are listed in Table 2.

It can be seen from Table 2, that the good linearity ($R^2 > 0.98500$) indicates that it is valid to illustrate the investigated decomposition process by the Avrami equation [Eq. (5)]. Also, it can be observed that the values of the Avrami rate constant ($K_A$) increased as the operating temperature increased, which directly suggests the following facts: the higher operating temperature, the faster the decomposition process, which is in good agreement with the general rule of chemical reactions.

The values of the Avrami constant ($n$), describing the isothermal decomposition, depend on the operating temperature for considered ferrite system (Table 2). At the lowest operating temperature (600 °C), the $n$ value is very close to $n = 3.00$ [$\sim$2.96 (Table 2)], while at a higher operating temperature (750 °C), the $n$ value increases to around $n = 4.00$ [$\sim$3.78 (Table 2)]. However, at the highest operating temperatures (including here the operating temperatures of 950 and 1,150 °C), the $n$ values exceeding $n = 4.00$, which achieves the highest value of $n = 4.74$ at 1,150 °C (Table 2). Normally, $n$ should not exceed 4 (i.e. the value for three-dimensional bulk nucleation). In the latter case, it can be assumed that the surface induced abnormal grain growth expected for Fe crystallization compounds [41] is responsible for the high value of $n$ for advanced crystallization at high operating temperatures ($T \geq$ 950 °C).

As we have known, the Avrami constant provides qualitative information on the nature of the nucleation and the growth processes in the overall crystallization, and may be changed. This fact of change in $n$ (Table 2) may imply that a change occurs in the decomposition mechanism, during the transition from a lower to a very high value area of the operating temperatures.

In the case of operating temperature of 600 °C, for which we have the value of $n = 2.96$ ($\approx$3.00) (Table 2), we can expect that the two-dimensional (2D) crystallization mechanism with a disc growth exists. The Avrami

**Table 2** Values of $n\ln K_A$, $\ln K_A$, $K_A$ and $n$ calculated from the linear dependence of $\ln[-\ln(1-\alpha)]$ against $\ln t$ at different operating temperatures (600, 750, 950, 1,150 °C) in considered conversion ranges (Δα), for Zinc–Iron-intermetallic phase decomposition process

| $T$ (°C) | Conversion range, Δα (−) | $n\ln K_A$ | $\ln K_A$, $K_A$ (min$^{-1}$) | $K_A$ (min$^{-1}$) | $n$ | $R^{2a}$ |
|---|---|---|---|---|---|---|
| 600 | 0.15–0.95 | −10.09495 | −3.41046 | 0.03303 | 2.96 ± 0.03 | 0.99165 |
| 750 | 0.15–0.95 | −12.32582 | −3.26080 | 0.03836 | 3.78 ± 0.05 | 0.99210 |
| 950 | 0.15–0.95 | −13.75917 | −3.18499 | 0.04138 | 4.32 ± 0.07 | 0.99198 |
| 1,150 | 0.15–0.95 | −14.94514 | −3.15298 | 0.04272 | 4.74 ± 0.09 | 0.98775 |

[a] Adj. $R^2$

**Table 3** The dimensionality and nucleation indexes ($d$ and $m$) with a qualitative description of crystallization phenomena identified for the isothermal decomposition process of Zinc–Iron-intermetallic phase, at the operating temperatures of 600 °C, 750 °C, 950 °C and 1,150 °C

| $T$ (°C) | $d$ | $m$ | $d + m$ | Nucleation mechanism | The nucleation rate over crystallization time |
|---|---|---|---|---|---|
| 600 | 1.96 | 0 | 1.96 | Sporadic (disc) | Steadily increasing with time |
| 750 | 3.00 | −0.22 | 2.78 | Instantaneous and sporadic (sphere) | Gradually decreasing with time and approaching a constant value |
| 950 | 3.00 | 0.32 | 3.32 | Sporadic (sphere) | Increasing with time |
| 1,150 | 3.00 | 0.74 | 3.74 | Sporadic (sphere) | Increasing with time |
| Average | 2.74 | 0.21 | 2.95 | Sporadic (sphere) | Increasing with time |

constant of $n = 3.00$ implies that the main crystallization mechanism is interface-controlled three-dimensional isotropic growth and early nucleation-site saturation. At the elevated operating temperature of 750 °C, where the value of $n = 3.78$ was identified, the investigated process proceeds through the three-dimensional (3D) crystallization mechanism, with a sphere morphological units [42]. In fact, the transformation for which $3 < n < 4$ (Table 2) is considered to imply that the process is interface-controlled with a decreasing nucleation rate [42]. On the other hand, an increasing nucleation rate with time can result in the value of $n > 4$ [43], as can be clearly seen for our investigated system at operating temperatures of 950 and 1,150 °C (Table 2).

### 4.4 The Dimensionality and Nucleation Index Analyses

Based on the obtained values of $n$, the corresponding values of dimensionality and nucleation index were estimated, by application of Eq. (9a). For investigated decomposition process, the values of $d$ and $m$, together with a qualitative description of crystallization phenomena at the different operating temperatures, are listed in Table 3.

From Table 3 we can see that an increase in operating temperature leads to changes in the dimensionality ($d$) and the nucleation index ($m$) values, where apparently there is a change in the nucleation mechanism, as well as in the nucleation rate behavior. This is also reflected through the character of the nucleation index ($m$), which maintains a zero value and the negative value at the operating temperatures of 600 °C and 750 °C, and then becomes positive above 750 °C. It should be noted that the operating temperature range, which is responsible for this change in the crystallization mechanism, is located above the value of 750 °C ($T > 750$ °C). Based on the average values of $d$ and $m$ (Table 3), we can conclude that the dominant crystallization mechanism (over the entire observed $T$ range) is the sporadic nucleation with a three-dimensional (3D) sphere growth of new phases.

Table 4 shows the relationships between $E_G$ and $E_N$ in the *apparent* (*effective*) activation energy for the decomposition process of Zinc–Iron-intermetallic phase, at the different operating temperatures (600 °C, 750 °C, 950 °C and 1,150 °C). The same table also shows the overall (averaged) relation for the effective activation energy with the corresponding contributions of the activation energies for the growth and nucleation processes, respectively.

**Table 4** The specific relationships between $E_G$ and $E_N$ contributions to the apparent (*effective*) activation energy for Zinc–Iron-intermetallic phase decomposition process, at the different operating temperatures (600 °C, 750 °C, 950 °C and 1,150 °C) [Relationships are derived on basis of Eq. (10)]

| $T$ (°C) | Effective activation energy for crystallization, $E_a$ (kJ mol$^{-1}$)[a] |
|---|---|
| 600 | $(2/3)\cdot E_G + (1/3)\cdot E_N$ |
| 750 | $(14/19)\cdot E_G + (5/19)\cdot E_N$ |
| 950 | $(10/13)\cdot E_G + (3/13)\cdot E_N$ |
| 1,150 | $(15/19)\cdot E_G + (4/19)\cdot E_N$ |
| Average | $(3/4)\cdot E_G + (1/4)\cdot E_N$ |

[a] The relationships were most closely calculated, since the $(d + m + 1)$ are non-integers

It can be observed from Table 4, that on all operation temperatures, the contributions of $E_G$ and $E_N$ to the apparent (*effective*) activation energy ($E_a$) of the investigated process, are exactly the fractional. It can be seen that an increase in operating temperature causes an increase in fractional values of $E_G$, while at the same time there is a decrease in fractional values of $E_N$. This behavior of $E_G$ and $E_N$ in $E_a$ for the overall investigated process, may indicate *secondary nucleation and growth* processes, especially at the lower super-saturation (this state can occurs in the presence of a foreign substrate, which can lead to a decline in the surface free energy ($\sigma$), and therefore lead to a reduction of $r^*$ (critical nuclei radius) and $\Delta G^*$ (the Gibbs free energy of formation of a nucleus of critical size) values [44], making nucleation more favorable). We can assume that in our case, the probability for the occurrence of this phenomenon increases with increasing of the operating temperature (Table 4).

However, the average relationship in the form of $E_a = (3/4)\cdot E_G + (1/4)\cdot E_N$ (Table 4) corresponds to 3D bulk nucleation and growth, where the crystals nucleate continuously at a constant rate $I$ throughout the transformation and the crystals grow as spheres at a growth rate $U$,

with the Avrami constant $n = 4$. In that case, the composite Avrami rate constant ($k_A$) can be expressed as [45]:

$$k_A = d \cdot C_d \cdot I \cdot U^d \cdot B(m+2,d) = 3 \cdot C_3 \cdot I \cdot U^3 \cdot B(m+2,d) \quad (36)$$

where $d$ is the *geometric index* ($d = 3$ for spheres) and $C_d$ is the *shape factor* ($C_3 = 4\pi/3$). The function $B(m + 2,d)$ represent the so-called $B$-function in the form:

$$B(m+2,d) = \int_0^1 q^{m+2-1}(1-q)^{d-1}dq, \quad (37)$$

which has a definite value for a given crystallization process and can be solved through numerical integration. If we consider the averaged results which are presented in Tables 3 and 4, we will have the following values of crystallization parameters: $d = 3$, $C_3 = (4\pi/3)$, and $m \approx 0$ (the value of $m = 0.21$ (Table 3) is approximated by zero, $m \to 0$, in order to estimates the finite value of $B$-function). In this case, the $B$-function has the form $B(2,3) = 1/(d + 1)d = 1/12$ [45].

For the considered case, the composite Avrami rate constant will take the following form:

$$k_A = \frac{\pi}{3} \cdot I \cdot U^3. \quad (38)$$

More generally, Eq. (38) refers to the case where the present a pre-determined nucleation of growth centers followed by a three-dimensional growth of the crystallites.

Considering the Avrami equation [Eq. (5)], the fraction of transformation (α) for the overall process (keeping in mind averaged values of crystallization parameters) can be expressed in the form:

$$\alpha = 1 - \exp\left[-\frac{\pi}{3} \cdot I \cdot U^3 \cdot t^4\right]. \quad (39)$$

At this point, it should be noted, that the composite Avrami rate constant shown in Eq. (38) relates to the Avrami rate constant ($K_A$) shown in Eq. (5), according to the main relationship $k_A = K_A^n$.

### 4.5 Analysis of the Behavior of the Local Avrami Constant [$n(\alpha)$]

Fig. 4 shows the local Avrami constant [$n(\alpha)$] values as a function of α, for Zinc–Iron-intermetallic phase decomposition, at the different operating temperatures. The local Avrami constant is not considered for a fraction of transformation lower than 0.05 (5 %) or higher than 0.95 (95 %) because of large error.

For investigated process at 600 °C, the value of $n(\alpha)$ decreases (from very high values that $n(\alpha) = 10.32$) with the fraction of transformation between 0.05 (5 %) and 0.70 (70 %), and stabilizes after the fraction of transformation exceeds 0.70 (70 %). This behavior indicates that the crystallization process is mainly governed by two-dimensional growth [20], where the high value of $n(\alpha)$ at the initial stage indicates, that the nucleation and consequently growth (in two dimensions) process begins (thereby causing that $n(\alpha)$ has a fairly high value). With the progress of crystallization, the $n(\alpha)$ decreases and approaches the value of approximately $n(\alpha) = 3.00$ (the value of $n(\alpha)$ in a steady-state condition is marked with a *blue* $n_{steady} = 2.60$ in Fig. 4). Decreases of $n(\alpha)$ values shows decrease of the increasing rate of nucleation, which may be attributed to the nucleation saturation. In this stage, two-dimensional growth of crystalline nuclei dominates, and the value of local Avrami constant tends to 3.00 [46]. According to theory of solid-state kinetics, if nucleation sites are small enough, the controlling mechanism must be the interface reaction because of the limited area of the interface, and because the distance over which the diffusion is necessary tends to zero [47]. However, when particles grow sufficiently, diffusion becomes the limiting factor. The interface-controlled growth model, in steady-state conditions gives the Avrami constant equal to 3.00. At the higher operating temperatures, above 600 °C, the variation of $n(\alpha)$ values with the fraction of transformation (α) in the initial stage, has the same form as the variation of $n(\alpha)$ values at $T = 600$ °C. However, in these cases, the local Avrami constant reaches the steady-state for the value, which is higher than $n = 3.00$ (Fig. 4). At the operating temperature of 750 °C, between 0.55 (55 %) and 0.90 (90 %), the $n(\alpha)$ is totally stabilized with the value of $n_{steady} = 3.40$ (the value of $n(\alpha)$ in a steady-state condition is marked with a

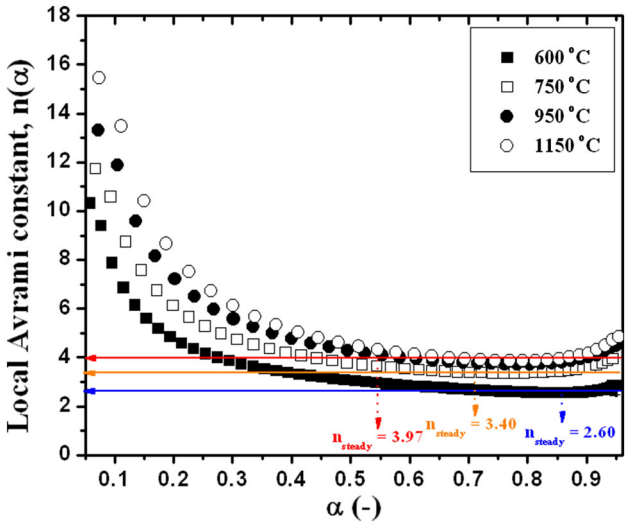


**Fig. 4** Relationship between the local Avrami constant [$n(\alpha)$] and the fraction of transformation (α), for Zinc–Iron-intermetallic phase decomposition process, at the different operating temperatures (steady state values are designated by $n_{steady}$)

*orange* $n_{steady} = 3.40$ in Fig. 4). Taking into account the obtained result, we can say that as the crystallization proceeds, the value of $n$ increases (compared to the value of $n$ at the operating temperature of 600 °C) and tends to an average value of about 3.40, indicating that a three-dimensional nucleation and growth process becomes dominating, of which the theoretical value of $n$ should be within 3.00–4.00 [20]. We suggest that in this stage of transformation, three-dimensional nucleation and growth of the spherical crystallites inside the bulk of the sample might be occurring.

At the operating temperatures of 950 and 1,150 °C, for the range of the fraction of transformation between 0.60 (60 %) and 0.90 (90 %), the $n(\alpha)$ values almost coincide in a single value of $n_{steady} = 3.97$ ($\approx$4.00) (the value of $n(\alpha)$ in a steady-state condition is marked with a *red* $n_{steady} = 3.97$ in Fig. 4). The value of $n = 4.00$ means that the investigated transformation occurs in a three-dimensional mode with a constant nucleation rate and a constant growth rate [20]. As a general conclusion that can be expressed on the basis of changes in $n(\alpha)$ values with increasing of $\alpha$, is that the nucleation rate is maximum in the initial stage of the process, and then nucleation rate decreases rapidly followed by growth of the product/products particles.

It should be noted, that the deviations of $n$ from the value of $n = 4.00$ (in terms of his overcoming) may be explained by a non-constant density of the growing crystals, at the higher operating temperatures. Namely, the "primary" (Avrami) and "secondary" (post Avrami) crystallization processes occurring in the sample may be described by the growth and subsequent relaxation of the crystalline regions, leading to a variable density within the sample.

### 4.6 The Correlation Between the Avrami Constant and the Effective Activation Energy Profile

In addition, based on Eq. (10), the values of the Avrami constant $n$ and the effective activation energies can be plotted in one graph as shown in Fig. 5.

The effective activation energy ($E_a$) for a wide range of $d$ and $m$ modes with Arrhenius temperature dependence can be expressed by Eq. (10). From Fig. 5 we can see that the calculated values of $E_a$ [Eq. (10)] decreases with the obtained values of $n$, showing a rising trend. In the variable range of the Avrami constant $n$, where extends from 2.90 to 4.63, the $E_a$ value decreases up to extremely low value equal to 0.8 kJ mol$^{-1}$. It can be observed three regions (Region I, II and III; Fig. 5) with characteristic changes in $E_a$ and $n$ values. Namely, in the Region I which corresponds to the variation of $n$ values in the range of 2.90–3.38 (in this case we can expect that *in this region there is likely the growth of pre-existing nuclei proceeds parallel with the nucleation process*), there appears the change in the values of $E_a$ from 8 to 6 kJ mol$^{-1}$. Region I belongs to the lower operating temperature region for $T = 600$ °C (Fig. 5). In the Region II, which corresponds to the medium operating temperature region (for $T = 750$ °C), we have a change of $n$ values in the range of 3.38–4.00 (in this case we can expect that *the crystallization proceeds through thermal nucleation and three-dimensional spherical growth*; since in this region the value of $n$ goes to $n = 4.00$ (Fig. 5), this means that *the crystallization mechanism is spherule growth from sporadic nucleation, with a reduced nucleation rate* [48]), where the change in the values of $E_a$ from 6 to 3.7 kJ mol$^{-1}$ exists. Finally, in the Region III, belonging to the higher operating temperature region (for $T = 950$ and 1,150 °C; Fig. 5), the Avrami constant exceeds the value of $n = 4.00$, so that changes in the range of 4.07–4.63, and this change in $n$, corresponding to the changes in the value of $E_a$ from 3.3 to 0.8 kJ mol$^{-1}$. In the considered region (for Region III in Fig. 5), we suggest the following mechanistic interpretation of the decomposition process at very high temperatures ($T > 950$ °C): Having in mind that the value of $n$ in a given region varies over $n = 4.00$ (when $n$ exceeds 4.00), the crystallization of probably presented » *amorphous* « phase (which is formed on the observed operating temperatures) should take place in the *autocatalytic stage* of the crystallization process, under the conditions where the rate of nucleation rapidly increases.

The full red line in the Fig. 5 represents the fit curve of Eq. (10), where the values of $E_N$ and $E_G$ can be calculated. Applying the averaging procedure, the following values were

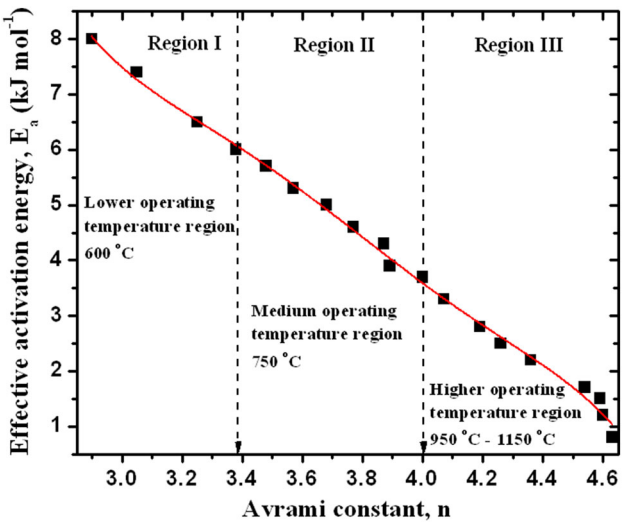


**Fig. 5** The effective activation energy ($E_a$) versus the Avrami constant ($n$). The full red line in the same figure represents the fit curve of Eq. (10), which was calculated using the averaging procedure. The corresponding reaction regions (designated by I, II and III) are also presented

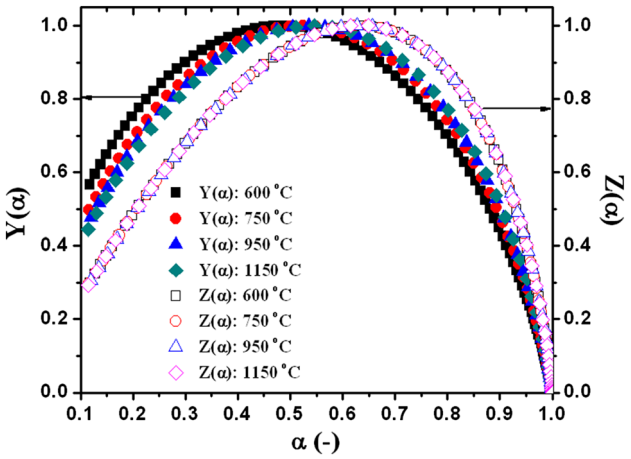


**Fig. 6** Normalized $Y(\alpha)$ and $Z(\alpha)$ functions [0,1], for Zinc–Iron-intermetallic phase decomposition process, at the different operating temperatures (600 °C, 750 °C, 950 °C and 1,150 °C)

found: $<E_N> = 3.9$ kJ mol$^{-1}$ and $<E_G> = 4.4$ kJ mol$^{-1}$, for the activation energies of the nucleation and growth, respectively.

Based on these results, we can conclude that the extremely low value of $E_a$ at the beginning of the decomposition process (at low values of $\alpha$ and for $n > 4.00$) (Figs. 3, 5) is due to the very low effective activation energy needed for the primary crystallites nucleating from the zinc ferrite matrix. In addition, this fact can be confirmed by a significant lowering of the energy barrier for nucleation [which is reflected in the small values of $E_N$ ($< E_N > = 3.9$ kJ mol$^{-1}$)], compared to the same for the growth ($< E_G > = 4.4$ kJ mol$^{-1}$). The high nucleation rate can be attributed to the formation of both Zn and Fe rich regions which provide a high number of heterogeneous nucleation sites, especially for the crystallization process at high operating temperatures.

### 4.7 Validation of Reaction Mechanism

In order to test the validity of JMA theory to explain the investigated decomposition process, the two special functions, $Y(\alpha)$ and $Z(\alpha)$, were applied. The functions $Y(\alpha)$ and $Z(\alpha)$ were obtained from the isothermal experimental ($d\alpha/dt$) data, using Eqs. (16)–(17), and they are shown in Fig. 6.

The shape of $Z(\alpha)$ functions are practically invariant with respect to the operating temperature. On the other hand, the shape of $Y(\alpha)$ functions shows the variation with an operating temperature, where the variation is more manifested at the lower values of conversion ($\alpha < 0.45$) (Fig. 6). Since, the $Z(\alpha)$ function does not show the variation with operating temperature, this means that the analytical form of the function of reaction mechanism *does not change in the observed range of the operating temperatures* ($600 \leq T \leq 1{,}150$ °C) (in the above presented results, we have assumed that the entire decomposition process occurs by the crystallization mechanism in the framework of the JMA model).

**Table 5** Values of $\alpha_m$ and $\alpha_p^{\infty}$ for the normalized $Y(\alpha)$ and $Z(\alpha)$ functions [0,1], as well as the values of the Avrami constant ($n$) for Zinc–Iron-intermetallic phase decomposition process, at the different operating temperatures (600 °C, 750 °C, 950 °C and 1,150 °C); The values of the Avrami rate constant ($K_A$) calculated by Eq. (8) are also given

| $T$ (°C) | $\alpha_m$ | $\alpha_p^{\infty}$ | $n$ | $K_A$ (min$^{-1}$)[a] |
|---|---|---|---|---|
| 600 | 0.484 | 0.638 | 2.96 | 0.03303 |
| 750 | 0.521 | 0.623 | 3.79 | 0.03836 |
| 950 | 0.536 | 0.627 | 4.31 | 0.04137 |
| 1,150 | 0.546 | 0.649 | 4.75 | 0.04272 |

[a] Equation (8)

However, the variation of $Y(\alpha)$ function with an operating temperature indicates that the process is not simple, but that the investigated decomposition corresponds to a complicated process (which may includes parallel or consecutive processes). Each of these processes can be characterized by continuous variation in the values of the Avrami constant in different operating temperature regions. This is confirmed by the variation of the local Avrami constant and the effective activation energy values, with a conversion, $\alpha$.

The maximum of the $Z(\alpha)$ function is located at $\alpha_p^{\infty} \approx 0.632$, and, therefore, the curves in Fig. 6 evidently correspond to the JMA kinetic model. This is confirmed also by the shape of the $Y(\alpha)$ function, which exhibits a maximum ($\alpha_m$) below $\alpha_p^{\infty}$. Table 5 lists the values of $\alpha_m$ and $\alpha_p^{\infty}$ at the different operating temperatures.

From Table 5, we can see that the value of $\alpha_m$ increases with an increasing of the operating temperature, while the values of $\alpha_p^{\infty}$ clearly indicate on the presence of the JMA kinetic model. The values of the Avrami constant ($n$) at the different operating temperatures are also calculated. These results are also shown in Table 5. It can be observed that the values of the Avrami constant are in excellent agreement with the values of the Avrami constant, presented in Table 2 (which are calculated from the dependence of $\ln[-\ln(1-\alpha)]$ against $\ln t$).

To check the validity of the obtained values for $K_A$ (Table 2) and the JMA kinetic model with the appropriate values of $n$, the kinetic method based on the Eq. (8) was applied. Figure 7 shows the linear dependence of $[-\ln(1-\alpha)]^{1/n}$ against $t$, for $n = 2.96$, 3.78, 4.32 and 4.74 at $T = 600$, 750, 950, and 1,150 °C, in the case of the decomposition process of zinc ferrite from neutral leach residues.

Based on the obtained super-correlations in linear plots ($R^2 = 1$) at all operating temperatures, from the slopes of the straight lines (Fig. 7), the corresponding values of $K_A$ were calculated. The obtained values for $K_A$ are presented in Table 5. It may be noted that these values (Table 5) are

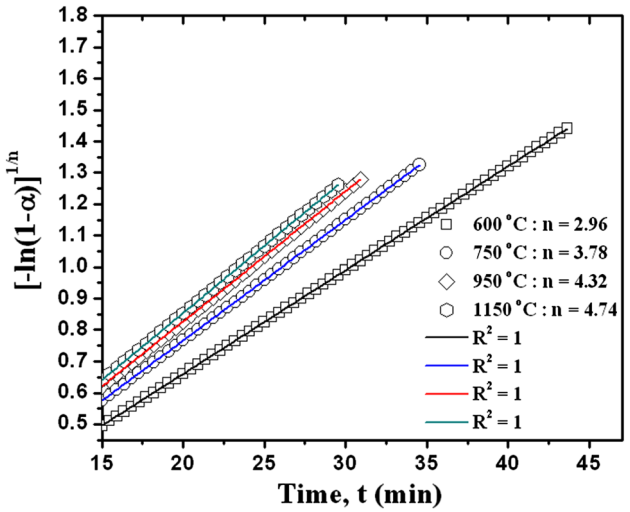


**Fig. 7** The linear dependence of $[-\ln(1-\alpha)]^{1/n}$ versus $t$, for $n = 2.96$, 3.78, 4.32 and 4.74 at $T = 600$, 750, 950, and 1,150 °C

fully consistent with the values of $K_A$ calculated on the basis of dependency $\ln[-\ln(1-\alpha)]$ versus $\ln t$ (Table 2).

From the Arrhenius dependence $\ln(K_A)$ as a function of $1/T$, the corresponding values for the *overall apparent* activation energy ($E_a$) and the *overall pre-exponential factor* ($k_o$) can be calculated, from the slope and the intercept of the obtained straight line, respectively. For the presentation of the term $\ln(K_A)$, the values of $\ln K_A$ from Table 2 were used. The following values of $E_a$ and $k_o$ were obtained: $E_a = 4.8 \pm 1.9$ kJ mol$^{-1}$ and $k_o = 0.0656$ min$^{-1}$. The estimated value of $E_a$ corresponds to the approximate value of $E_a = 4.9$ kJ mol$^{-1}$ at $\alpha = 0.65$ in Fig. 3. The calculated value of $E_a$ is higher than the corresponding average values for $E_N$ and $E_G$. The value of $E_a$ can be calculated from the half-time ($t_{0.50}$) values, and the derived value can then be compared with the value obtained on the basis of the direct Arrhenius dependence. Significant features of the investigated process, which are based on the behavior of $t_{0.50}$ and $t_{max}$ magnitudes, will be discussed in the next subsection.

### 4.8 Consideration of Behavior of $t_{0.50}$ and $t_{max}$ Terms for Zinc–Iron-Intermetallic Phase Decomposition

Half-time analysis and linear least squares analysis should yield consistent results and allow one to quantify isothermal rates of crystallization via generalized Avrami equation. The maximum rate of crystallization ($v_{max}$) can be evaluated when $t = t_{max}$, so that we have:

$$v_{\max} = \left\{\frac{d}{dt}\left[\frac{\alpha(t;T)}{\alpha(t\to\infty)}\right]\right\}_{t=t_{\max}} = nk_A t_{\max}^{n-1}\exp\left(-k_A t_{\max}^{n}\right) = \Omega(n)\cdot k_A^{\frac{1}{n}}, \quad (40)$$

where

$$\Omega(n) = (n-1)^{\frac{(n-1)}{n}}\cdot n^{\frac{1}{n}}\cdot\exp\left[-\frac{(n-1)}{n}\right] \quad (41)$$

and $\Omega = 1$, when $n = 1$. One identifies $k_A^{1/n}$ as the Avrami rate constant $K_A$, with dimensions (time)$^{-1}$. Taking into account Eqs. (15), (40) and (41), the maximum rate of crystallization can be expressed in the form:

$$v_{\max} = \left\{\frac{d}{dt}\left[\frac{\alpha(t;T)}{\alpha(t\to\infty)}\right]\right\}_{t=t_{\max}} = \Omega(n)\cdot k_A^{\frac{1}{n}} = \frac{\Omega(n)\cdot(\ln 2)^{\frac{1}{n}}}{t_{0.50}}. \quad (42)$$

The $t_{0.50}$ and $t_{max}$ represent the important parameters for consideration of the entire decomposition process of zinc ferrite from neutral leach residues, under isothermal experimental conditions. It can be pointed out, that the half-time parameter ($t_{0.50}$) can be obtained in two ways: (a) determined for each of the operating temperature, directly from the experimental $\alpha$–$t$ curves (designated by $t^*_{0.50}$), and (b) using the Avrami rate constant values.

Table 6 lists the values of $t_{0.50}$, $t^*_{0.50}$, $t^{-1}_{0.50}$ (the reciprocal half-time), $t_{max}$, $t_{max}/t_{0.50}$, $\Omega(n)$ and $v_{max}$, at the different operating temperatures (600 °C, 750 °C, 950 °C and 1,150 °C).

It can be seen from Table 6, that the half-time ($t_{0.50}$) (also and $t^*_{0.50}$) is greater than $t_{max}$ when $n < 3.26$ [only in this case, the ratio $t_{max}/t_{0.50}$ is less than unity (Table 6)], and $t_{0.50}$ occurs prior to the inflection point of the $\alpha$–$t$ curve when $n > 3.26$, but differences between $t_{0.50}$ and $t_{max}$ could be difficult to resolve for reasonable values of $n$ between 3.00 and 4.00. Namely, the half-time ($t_{0.50}$) is coincident with the inflection point of $\alpha$–$t$ curve, only in the case of perfect symmetry, realized on the true determined value, which is $n = 3.26$ (this corresponds to the symmetrically centered Gaussian distribution, which is identical to the Weibull distribution with shape parameter equal to $\beta = 3.26$), and which implies that $t_{0.50} = t_{max}$. Given that at the operating temperatures above 600 °C, the value of $n$ is greater than 3.26 (Tables 2, 5), then we can clearly see that the $t_{max} > t_{0.50}$ (and the ratio $t_{max}/t_{0.50} > 1$) (Table 6).

Based on the obtained results, it follows that the overall crystallization rate ($v_{max}$) is achieved much faster, when the operation temperature exceeds 600 °C, and it reaches its maximum value at the highest operating temperature (1,150 °C) (Table 6).

It can be pointed out, that the larger half-time indicates a slower crystallization rate (the growth rate ($U$) can be approximated by $t^{-1}_{0.50}$ (Table 6) i.e., $U \sim t^{-1}_{0.50}$). Figure 8 shows the trends of half-time ($t_{0.50}$) and the reciprocal half-time ($t^{-1}_{0.50}$) [the crystal growth rate ($U$)] as a function of the operating temperature.

**Table 6** Summary of the calculated half-time ($t_{0.50}$), experimental half-time ($t^{*}_{0.50}$), the reciprocal half-time ($t^{-1}_{0.50}$), the maximum time ($t_{max}$) (which corresponds to the inflection point of the $\alpha$–$t$ curve), the ration ($t_{max}/t_{0.50}$), the function $\Omega(n)$ [Eq. (41)] and the maximum rate of the overall crystallization ($v_{max}$) [Eq. (42)] values, at the different operating temperatures (600 °C, 750 °C, 950 °C and 1,150 °C)

| $T$ (°C) | $t_{0.50}$ (min) | $t^{*}_{0.50}$ (min) | $t^{-1}_{0.50}$ (min$^{-1}$) | $t_{max}$ (min) | $t_{max}/t_{0.50}$ | $\Omega(n)$ | $v_{max}$ (min$^{-1}$) |
|---|---|---|---|---|---|---|---|
| 600 | 26.749 | 26.658 | 0.03738 | 26.339 | 0.985 | 1.16190 | 0.03838 |
| 750 | 23.660 | 23.256 | 0.04227 | 24.033 | 1.016 | 1.44526 | 0.05544 |
| 950 | 22.201 | 21.995 | 0.04504 | 22.737 | 1.024 | 1.63623 | 0.06771 |
| 1,150 | 21.665 | 21.116 | 0.04615 | 22.267 | 1.028 | 1.78612 | 0.07630 |

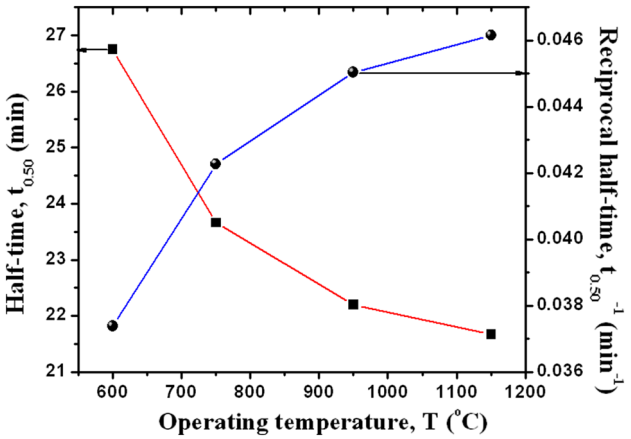


**Fig. 8** The trends of half-time ($t_{0.50}$) and the reciprocal half-time ($t^{-1}_{0.50}$) value, as a function of the operating temperature ($T$)

The behavior of $t_{0.50}$ and $t^{-1}_{0.50}$ with increasing of the operating temperature corresponds to the same class of the functions, which is a class of the *exponential* functions. However, this dependence does not belong to the same category of the exponential functions.

Based on the presented results, we can conclude that at the highest operating temperature (1,150 °C), the highest possible crystallization rate for the investigated process is achieved. Also, at the mentioned operating temperature, the rate of formation of the crystal grains is the largest.

Here, it should be noted, that in Fig. 8 we can not see the emergence of a minimum in $t_{0.50}$ at a given value of $T$, which lay between the glass transition temperature ($T_g$) (if we considered the cases for *metal compounds*) and melting temperature ($T_m$), where they formed the so-called bell-shaped curve of the isothermal crystallization (It is often the case for the polymer crystallizations). Namely, for example, the extraction of ZnO (followed by zinc extraction in hydrometallurgical processing) is usually carried out below the melting points of the sulfides and oxides involved, usually below 1,200 °C (for example, for willemite ($Zn_2SiO_4$), the melting temperature is $T_m$ = 1,512 °C, while for hematite ($Fe_2O_3$), $T_m$ is equal to 1,566 °C). On the other hand, in order for the reactions to occur with a sufficient velocity, the operating temperature has to be above 500–600 °C [49]. Thus, the operating temperature range of interest is between 500 °C and 1,200 °C.

Additionally, the *apparent* activation energy ($E^{0.50}_a$) and the *apparent* pre-exponential factor ($k^{0.50}_o$) can also be obtained from the linear dependence $\ln(t^{-1}_{0.50}) = \ln k^{0.50}_o - E^{0.50}_a/RT$. The *apparent* activation energy ($E^{0.50}_a$) value calculated is $E^{0.50}_a = 4.0 \pm 0.9$ kJ mol$^{-1}$, while the value of $k^{0.50}_o$ was calculated with the value of $k^{0.50}_o = 0.0655$ min$^{-1}$. These values are in good agreement with the values that were obtained from the dependence $\ln(K_A)$ versus $1/T$ ($E_a = 4.8 \pm 1.9$ kJ mol$^{-1}$ and $k_o = 0.0656$ min$^{-1}$). Also, these *apparent* activation energy results demonstrate the fact, that both approaches can be utilized to determine the apparent activation energy for the investigated decomposition process.

### 4.9 The Mechanistic Aspects

Figure 9 shows the current reactions scheme in terms of corresponding operating temperature regions, in which the observed reactions occurring within the complex Zinc–Iron-intermetallic phase decomposition.

As the main product of decomposition process at the elevated temperatures, is the zincite (ZnO), which can be further, transformed by smelting process into zinc. The above process may include the gas–solid reactions at the elevated operating temperatures, which precedes smelting in pyrometallurgy and leaching in hydrometallurgy. For our tested process, we can assume the system of parallel reactions, which proceed in the respective operating temperature regions, just set out in Fig. 9.

It was found that the reduction of hematite to magnetite may be accompanied by the formation and growth of nuclei model or the phase-boundary reaction model, respectively, depending on the operating temperature range [50, 51]. The XRD investigations showed the dependence of reduction route on the operating temperature [50, 51].

Given the physical nature of the original sample, and the chemical composition of the final decomposed materials,

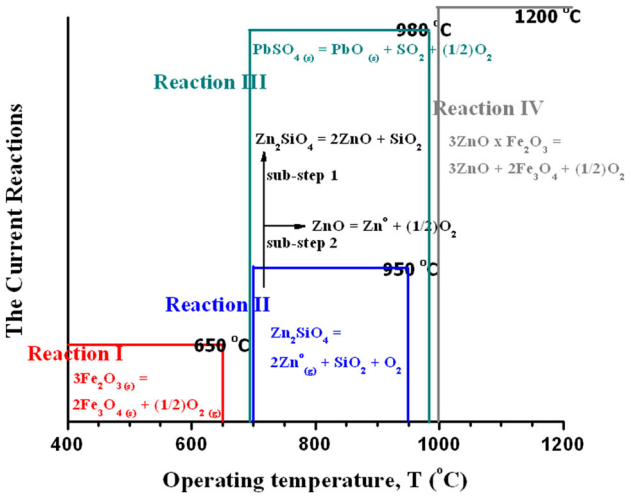


**Fig. 9** Current reactions scheme in terms of corresponding operating temperature regions, in which the observed reactions occurring within complex Zinc–Iron-intermetallic phase decomposition process

we will take a look at a general chemical equation, which is represented by reaction I in Fig. 9. It should be noted that the range of operating temperatures that are used, as well as the partial pressure of oxygen can strongly affect on the reduction rate. It has been shown that the relatively low operating temperature (450–600 °C), and rather high partial pressures of oxygen ($O_2$) significantly accelerate the transformation of $Fe_2O_3$ into $Fe_3O_4$ ($Fe^{2+}$ becomes much more stable in relation to $Fe^{3+}$ at decreasing of partial pressure of $O_2$) [52]. We believe that the operating temperature of 600 °C is ideal for the transformation that takes place by the reaction I (Fig. 9). In fact, no matter what the process in "reaction I" takes place in a system of several parallel reactions, we believe if it came to a complete formation of metallic iron, from wüstite (FeO) transformation, in that case it would probably show a greater variation (by means of *amplitude of variation*) of $E_a$ with α (in the sense of certain *decrease* in the value of $E_a$, at a certain value of α). Such behavior is not observed in Fig. 3. It was shown, that in the kinetic study of $Fe_2O_3$ reduction process, in the $T$ range from 300 to 740 °C, the gradual decrease of $E_a$ values can be detected [53]. Specifically, this decline in the $E_a$ values becomes greater with an increasing of α in the final stage of the reduction process beyond $\alpha = 0.80$ [53]. One of the reasons for this behavior is just the transformation of FeO during the reduction process. In the considered case, we can assume that at the operating temperature of 600 °C, the reduction of $Fe_2O_3$ into $Fe_3O_4$ is fairly fast (characterized by the steadily increasing of the nucleation rate) and seriously influenced by the percentage of oxygen deposition and external mass transfer, during the two-dimensional growth of magnetite nuclei into uniformly circular discs. This mechanism suggests that the reduction process at the considered operating temperature is controlled by interface-controlled kinetic model. Namely, according to the above mechanism, we can assume that in this case, we can expect that the magnetite initially forms as a surface layer on the hematite reactant, and then the gradually replaces the hematite. Nucleation of magnetite appears to be a highly favored process, as is attested by the rapid initial rate at which the hematite reduction takes place (this is confirmed by the results presented in Tables 2, 3 and 5 for 600 °C). Further, it can be assumed that the reduction process is probably initiated by hematite reaction with the carbon, which was present in the initial tested sample. It can be pointed out, that the reduction of hematite to magnetite is frequently accompanied by the formation of pores, which are preserved during subsequent reduction to wüstite. The size and distribution of these pores change with an operating temperature that was used. In this sense, the temperature conditions under which the magnetite is formed can play a vital role in the entire process.

The willemite decomposition process is presented by reaction II in Fig. 9. As a consequence, the interpretation of the course of the decomposition can be divided into two sub-steps (sub-step 1 and 2 in Fig. 9).

If we consider sub-step 1 (Fig. 9) (through the obtained kinetic results), the formation of ZnO from willemite transformation proceeds by process which is controlled by nucleation, and has the spherical structure. Namely, the zincite (ZnO) crystallization process probably occurs through the polyhedral crystal growth [54] mechanism (i.e., three-dimensional growth), where the value of $n$ approaches to $n = 4.00$. The next reaction sub-step (sub-step 2 in Fig. 9) occurs when incurred ZnO probably left a small open area between the $Zn_2SiO_4$ shell and the ZnO core. The vacuum in this open area facilitated the decomposition of the rest of zincite core to yield the Zn vapor and $O_2$ vapor at the operating temperatures above 800 °C (≈800–900 °C). We believe that in this case, $Zn_2SiO_4$ shell is not thin enough, so that the evolution of gaseous zinc and oxygen are not limited by diffusion through a solid matrix. It has to be kept in mind that ZnO decomposes into the elements below the melting point ($T_m^{ZnO} = 1{,}975$ °C) if the oxygen partial pressure is too low. This is important for the deposition of such type of oxides at the higher substrate operating temperatures. Namely, the vapor pressure of ZnO is high already at about 1,400 °C, which makes it difficult to grow single crystals from its own melt. The stoichiometric width of ZnO below 600 °C is rather narrow. For temperatures higher than 600 °C, Hagemark and Toren [55] measured the Zn–$Zn_{1+x}O$ phase boundary by an electro-chemical method, and conductivity measurements assuming that excess zinc constitutes a shallow donor in ZnO. The new

measurements performed by Tomlins et al. [56] suggest that Hagemark and Toren [55] actually measured the phase boundary Zn–$ZnO_{1-x}$ i.e., the concentration of *oxygen vacancies*. In that case, the oxygen vacancies can be generated in ZnO during crystallization. As a result, ZnO grew slightly faster and formed more rounded (in terms of surfaces) polyhedral structures [56].

The operating temperature range for anglesite ($PbSO_4$) decomposition is 750 °C < $T$ < 980 °C (Reaction III in Fig. 9). We may expect that lead sulphate decomposes very slowly with the formation of the basic salt $6PbO{\cdot}5SO_3$ at 700 °C. This salt undergoes a transformation at 850 °C, and begins to decompose at 880 °C, where the rapid dissociation begins at 950 °C, and is accompanied by volatilization of PbO [57]. Based on the established results, we can assume that in this case, probably exists a three-dimensional growth of the formed PbO particles, where the nucleation rate, after a certain time period, tends to reach a constant value. The exposed assumption is a typical for the case of obtaining of the large crystals, in the form of long and laminar structure [57].

The final production of zinc oxide (ZnO) is surely completed at the temperature of 1,200 °C (Reaction IV in Fig. 9). The catalytic complex as ZnO × $Fe_2O_3$, is split at the very high operating temperatures ($T$ > 1,000 °C) in a non-complex form as ZnO + $Fe_3O_4$ + 1/2$O_2$. The complex ZnO x $Fe_2O_3$ likely to be autocatalytic decomposed into ZnO and other chemical species, which significantly reduces the energy barrier for a given process. In the case of autocatalytic reaction, the reaction rate is strongly influenced by the concentration of the formed product. In the considered decomposition process, the overall decomposition reaction rate is strongly depends on the amount of the obtained zincite. It can be pointed out, that the rate of investigated process increases, when the nucleation process is autocatalytic, causing an increase in the value of the Avrami constant above $n = 4.00$ ($n > 4.00$). From the obtained results, we may conclude that the process which occurs at the operating temperatures $T \geq 950$ °C is surely proceeds through the autocatalytic reaction mechanism (Tables 2, 3, 5). This result indicates that the rate of nucleation abruptly increases, at a very early stage of the observed process.

Based on very high value of the Avrami constant, especially at $T = 1{,}150$ °C ($n = 4.74$, Table 2), we can expect the effect of branching, especially in response to the initial compound that has autocatalytic properties. In this case, we will have an extremely low value of $E_a$ (Fig. 5). The formation of the branches is the nucleation of new crystals on the columnar facets of ZnO crystals. One might expect the existence of the line defects under the branched crystals. These line defects that are created, serve as the pin-points for the secondary nucleation to occur. Branch growth on the single crystalline ZnO further supports the idea that the new crystals are mostly formed on the defect sites, such as edges or holes. Also, it should be noted that the increase in the operating temperature in Zn vapor did not result in a decrease of the existing in Zn constitutional vacancies. If Zn interstitials had diffused into the crystal, then one would have expected the open-volume *defects* to have been filled [58, 59]. Instead, Zn vapor may causes an increasing in O vacancies in the bulk by growing new ZnO on the surface. At this point, we should say that it was found, that the zinc pressure (through the vapor transport) can act auto-catalytically inducing $O_2$ and Zn partial pressures higher than the equilibrium ones, and promoting the decomposition process.

Figure 10 shows phase stability diagram for the system Zn–Fe–S–O and the process window changes for Zinc–Iron-intermetallic phase (ferrite) decomposition.

From the industrial point of view, principally two routes for Zinc–Iron-intermetallic phase (ferrite) decomposition exist: (a) (intensively) carbon addition with full Zn-evaporation at/below 900 °C and (b) an application of the moderate reducing conditions by avoiding carbon addition using inert gas. In the latter case the operation temperature has to be elevated to 1,100–1,200 °C allowing for decomposition according to Reaction IV (Fig. 9). In this case, the standard steel parts may still be applicable, which not possible in the presence of $SO_2$ (primary roasting). It should be noted, that due to the fact that insoluble zinc-ferrite can not be completely avoided, the solids ("iron–zinc concentrate") separated from the zinc-bearing solution by sedimentation and filtration contains significant Zn-concentrations.

After completion of the thermal decomposition process of the investigated sample, the presence of particles with

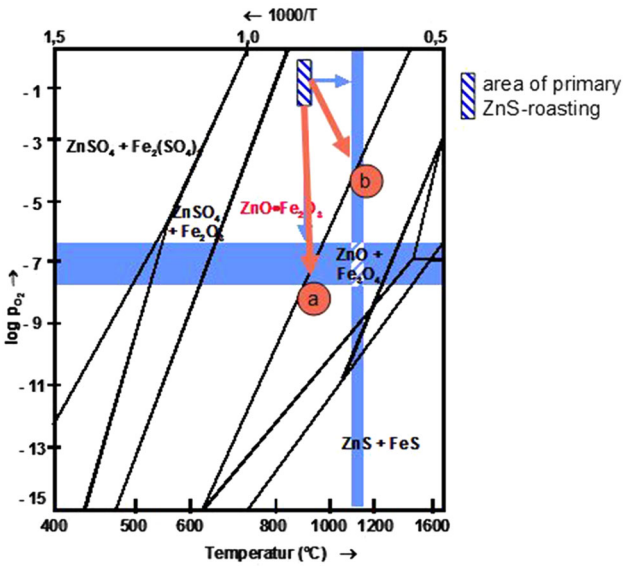


**Fig. 10** Phase stability diagram for the system Zn–Fe–S–O and process window changes for Zinc–Iron-intermetallic phase decomposition

different forms and sizes in a final structure was observed. The corresponding SEM image of the final representative sample after the thermal decomposition at the operating temperature of 1,150 °C is shown in Fig. 11.

Figure 11 clearly shows the existence of the specific areas containing the four different particle types. According to the obtained particle shapes, we can quite confidently assume that we have a strong presence of zinc after the decomposition ("Area 1" in Fig. 11), which indicates that there has not been intense evaporation. The "Area 1" shown in Fig. 11 is the dominant one. The second important area ("Area 2" in Fig. 11) can be attributed to the magnetite ($Fe_3O_4$) structure (namely, the iron is present only in the form of $Fe_3O_4$, and the final product, which underwent the decomposition, has the magnetic properties as the opposed to the original material [1]). The remaining two areas in Fig. 11 ("Areas 3–4", which are much less dominant [brighter parts in Fig. 11)], can be attributed to the remains of magnesium in the form of $Mg_2Si_2O_6$ and the possible presence of lead oxide particles, which was confirmed in our previous paper, using the energy disperse spectroscopy (EDS) [1].

### 4.10 Statistical Analysis

Based on the theoretical considerations, we calculate the corresponding values of distribution parameters ($\beta$, $\eta$ and $1/\eta$), using the Weibull probability plots (WPP) (in the same conversion ranges, as in the case of dependence $\ln[-\ln(1-\alpha)]$ against $\ln t$).

Table 7 lists the values of $\beta$, $\eta$ and $1/\eta$ at the different operating temperatures (600, 750, 950 and 1,150 °C), for Zinc–Iron-intermetallic phase (ferrite) decomposition.

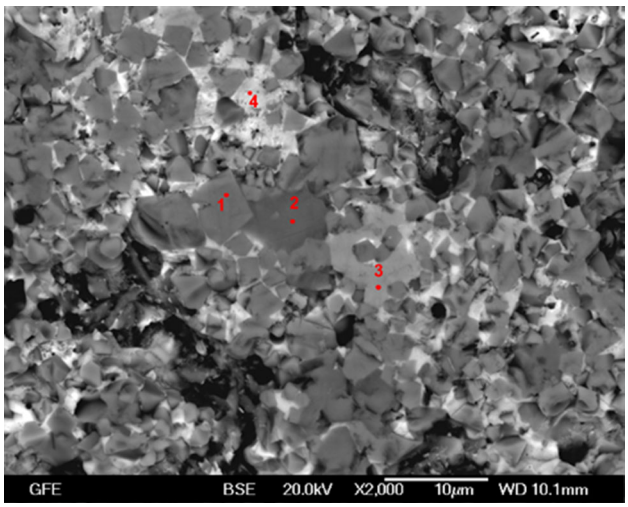


**Fig. 11** SEM image of the final representative sample, after the thermal decomposition at the operating temperature of 1,150 °C

**Table 7** Values of the Weibull distribution parameters ($\beta$ and $\eta$) as well as the values of characteristic rate constants ($1/\eta$), calculated using Eq. (29) at the different operating temperatures (600, 750, 950, 1,150 °C), for Zinc–Iron-intermetallic phase decomposition process

| $T$ (°C) | Conversion range, $\Delta\alpha$ (−) | $1/\eta$ ($\text{min}^{-1}$) | $\eta$ (min) | $\beta$ |
|---|---|---|---|---|
| 600 | 0.15–0.95 | 0.03303 | 30.28 | 2.96 |
| 750 | 0.15–0.95 | 0.03836 | 26.07 | 3.78 |
| 950 | 0.15–0.95 | 0.04138 | 24.17 | 4.32 |
| 1,150 | 0.15–0.95 | 0.04272 | 23.41 | 4.74 |

It can be seen from Table 7 that the value of the the scale parameter ($\eta$) decreases with an increasing of the operating temperature. The values of the shape parameter ($\beta$) show the same behavior with increase in the operating temperature, as in the case of changes in the value of the Avrami constant (Table 2). Also, Table 7 shows that the values of the characteristic rate constant ($1/\eta$) at all operating temperatures, are identical to the values of the Avrami rate constant (Table 2).

Many models have been used in the literature for the survival studies, and for example these are exponential, log-normal or Weibull. Exponential and log-normal models are not adequate for survival studies because in this context they lack physical meaning: in fact the survival function associated to the former is constant over time, while in the second model it shows a peak corresponding to the earliest values of the time variable. Both these shapes are incompatible with examination of the thermo-induced transformations in metal compounds, since the survival function is expected to increase with time variable [60]. This is why the Weibull distribution model has been chosen for discussion of the survival analysis in the case of Zinc–Iron-intermetallic phase decomposition.

One fundamental ideas in survival studies is that "components" (the "component" means any individual reactions within the complex decomposition process) do not all fail at the exact same time. Therefore, to compute an estimate of a decomposition *lifetime*, the statistical distribution of the failure times needs to be determined. Figure 12 shows the survival curves $S(t)$ which are derived from the cumulative hazard functions $H^*(t)$ (not shown), for investigated decomposition process, at the different operating temperatures ($T = 600$, 750, 950 and 1,150 °C).

From Fig. 12, we can draw the following conclusions:

a) If the maximum acceptable failure rate is 40 %, then the intersection of the 50 % survival probability with the curves at considered operating temperatures, suggest a lifetimes of 26.749, 23.660, 22.201, and 21.665 min, for $T = 600$, 750, 950 and 1,150 °C, respectively (Fig. 12). These values are fully consistent with the values of half-time ($t_{0.50}$) (Table 6). On the other hand, if the maximum

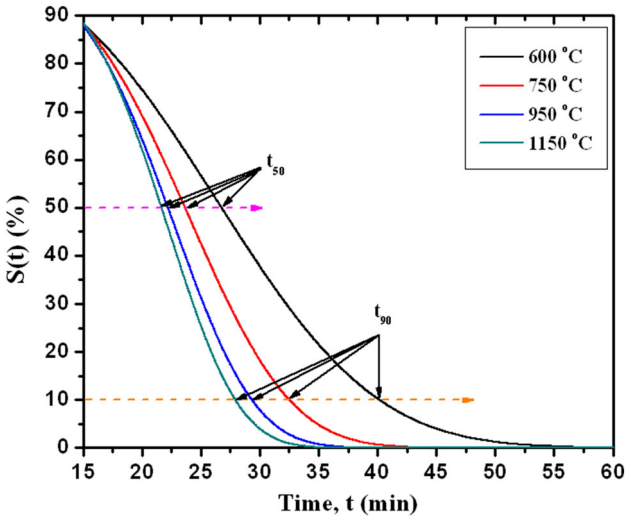


**Fig. 12** The survival curves $S(t)$ (derived from the cumulative hazard functions $[H^*(t)]$, for Zinc–Iron-intermetallic phase decomposition process, at the different operating temperatures (600, 750, 950 and 1,150 °C); In the same figure, the values of lifetimes at the considered operating temperatures, which correspond to 50 and 10 % survival probabilities ($t_{50}$ and $t_{90}$) are indicated by arrows

acceptable failure rate is 80 %, then the intersection of the 10 % survival probability with the observed curves, suggest a lifetimes of 40.109, 32.412, 29.234 and 27.854 min, for $T = 600$, 750, 950 and 1,150 °C, respectively (Fig. 12);

b) In our investigated case, we have $S(t_{50}) > S(t_{90})$ which implies $t_{50} < t_{90}$ (and vice versa) at all $T$'s, i.e., $S(t)$ declines monotonically.

c) From items (a) and (b) we can implicitly assumed that all "components" undergo the statistical event (in this case, it is the whole decomposition process), if they have enough reaction time. Given that all $S(t)$ curves are smooth (Fig. 12) and when $t \rightarrow \infty$ (approximately) (especially for $T = 600$ °C, where $S(t)$ curve is the longest) we will have that $S(t) = 0$, i.e., expressed mathematically in the form $lim_{\,t \rightarrow \infty}\, S(t) = 0$.

d) On the basis of the facts established under the item (c), we can confidently assert that all important products of decomposition (Sect. 4.9) reward after exactly 60 min from the start of monitoring the entire process (Fig. 12). This result is very important for establishing the process conditions, in order to target the industrial exploitation of zinc and zinc oxide.

It was found that the shape of $H^*(t)$ curve at every observed operating temperature, corresponds to the final part of the so-called *bathtub* curve (in fact, represents the so-called *third* or the *final period* on *bathtub* curve) [61]. This period is valid only for the values of shape parameter greater than unity ($\beta > 1$). This third period is the end-of-life period that exhibits an increasing failure rate. It was also found that $H^*(t)$ function reaches a maximum value at the maximum operating temperature (1,150 °C), which is consistent with the highest value achieved for the Avrami rate constant, $K_A$, attached to $n = 4.74$ (Table 2).

Based on Eq. (35), the distribution parameters $\beta_{E_a}$ and $\eta_{E_a}$ were calculated. The following values of distribution parameters were obtained: $\beta_{E_a} = 1.47 \pm 0.02$ and $\eta_{E_a} = 4.5 \pm 0.1$ kJ mol$^{-1}$. The energy plot (not shown) was characterized by a high value of $R^2$ (Adj. R-Square, $R^2 = 0.99692$).

Based on the obtained values of distribution parameters ($\beta_{E_a}$, $\eta_{E_a}$), the corresponding $F(E_a)$ and $f(E_a)$ functions were evaluated. Fig. 13 shows the calculated distribution functions $F(E_a)$ and $f(E_a)$.

It can be seen from Fig. 13, that the function $F(E_a)$ is characterized by the accelerating behavior, with a typical inflection point at coordinates: [27.4 % (expressed as a percentage), 2.1 kJ mol$^{-1}$]. Until the inflection point on a cumulative $F(E_a)$ curve, the density function $[f(E_a)]$ exhibits an increase (referring to the the probability of process realization, which is implicitly associated with the rate evaluation for the same process, in general) with increasing in $E_a$ values, and reaches its maximum value exactly at $F_{inf}(E_a^{max})$ point ($E_a^{max} = 2.1$ kJ mol$^{-1}$) (Fig. 13). After the inflection point, $F(E_a)$ curve exhibits a slow "growth" trend, with a density function $[f(E_a)]$ characterized by decrease in probability (with further increase in $E_a$ values), showing the appearance of a long right tail.

The increase in the probability of process realization, and the occurrence of the maximum of the $f(E_a)$ function at low values of $E_a$ (Fig. 13), strongly suggests on the autocatalytic behavior of a given system, as well as the presence of high nucleation rate, as previously indicated.

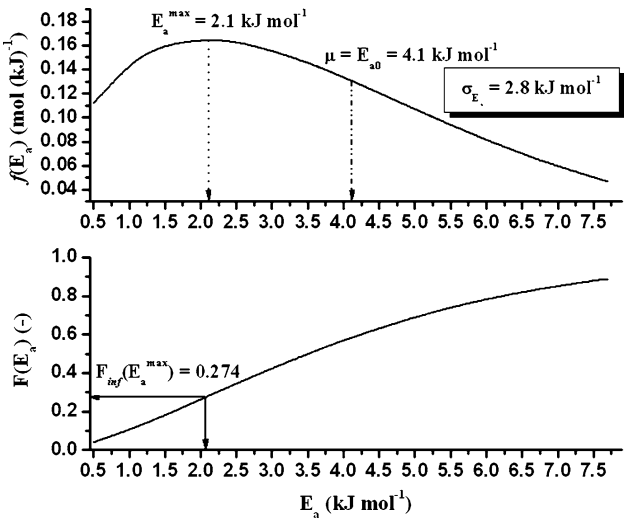


**Fig. 13** The distribution functions $F(E_a)$ and $f(E_a)$ for Zinc–Iron-intermetallic phase decomposition process; The inflection point is designated by $F_{inf}(E_a^{max})$ in $F(E_a) - E_a$ graph. Corresponding values for $E_a^{max}$, $\mu$, and $\alpha_{E_a}$ were presented in $f(E_a) - E_a$ graph

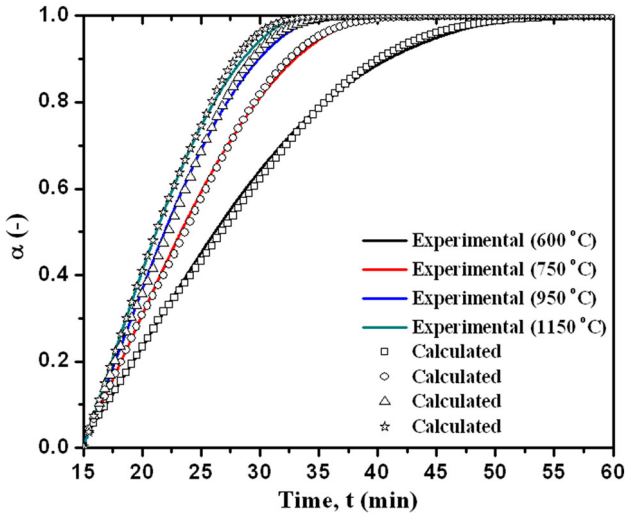


**Fig. 14** The comparison of the experimentally obtained conversion (α–*t*) curves (*full color lines*) with α–*t* curves which are calculated numerically (*symbols*), using the reactivity distribution model described by Eq. (30)

The calculated value of the mean apparent activation energy ($E_{ao} = 4.1$ kJ mol$^{-1}$) (Fig. 13) is close to the value corresponding to activation energy for *nucleation* process ($< E_N > = 3.9$ kJ mol$^{-1}$). Having in mind the full range of variation of the $E_a$ values during decomposition, the value of *dispersion* [$\alpha_{E_a} = 2.8$ kJ mol$^{-1}$ (Fig. 13)] shows a rather wide density distribution function, $f(E_a)$.

One of the important properties of the Weibull distribution is the flexibility, so depending on the parameter values, this distribution can approximate a large number of different distribution functions.

Based on the obtained value of $\beta_{E_a}$, it can be concluded that the main characteristic of the density distribution function of $E_a$ values, results from the fact that shape parameter in the range $1 < \beta_{E_a} < 2$ corresponding to skewed distribution. Applying the theory of probability and various statistical distributions, this distribution indicates increasing $E_a$ values of the process, with $E_a$ as the random variable (cumulative function in Fig. 13). From the shape of the density distribution functions presented in Fig. 13, we can conclude that the $f(E_a)$ function belongs to the group of *positively skewed distributions*. The skewness is a measure of the asymmetry of the probability function, with a real values of random variable. A positive skew indicates that the tail on the right side is longer than the left side and the "*bulk*" of the $E_a$ values lie left of the mean. This form of $f(E_a)$ function, together with all the above-mentioned features, represent so-called "*fingerprint*" distribution for the current process.

Figure 14 shows the comparison of the experimentally obtained conversion ($\alpha - t$) curves with α–*t* curves which are calculated numerically, using reactivity distribution model, described by Eq. (30). The values of the parameters used in calculation procedure were as the follows: $k_o = 0.0656$ min$^{-1}$, $\beta$'s from Table 7 at every considered operating temperature, together with the values of $E_a$ and $f(E_a)$, presented in Fig. 13.

Figure 14 shows that at all operating temperatures, there is a very good agreement between the experimental and the calculated conversion ($\alpha - t$) curves, using the proposed reactivity distribution model, which is given by Eq. (30). In the presented model, the density distribution function [$f(E_a)$], includes the autocatalytic behavior of the system, that contains a set of parallel reaction pathways, where the identified reaction channels significantly affect the apparent lowering the energy barrier for the emergence of the overall decomposition process.

## 5 Conclusions

The present study is primarily focused on the application of kinetic–statistical approach in order to investigate the complex mechanism of thermal decomposition of Zinc–Iron-intermetallic phase (ferrite), as by-product from the neutral leach residues. The application of this approach on the current process, has led to the following conclusions:

- The phase transformation kinetics showed that the investigated decomposition represents the complex process, which includes a set of parallel reactions (mostly gas–solid type reactions), which occur at different operating temperature ranges. This fact has been confirmed by varying the Avrami constant ($n$) with operating temperature, which at higher $T$ exceeds the value $n = 4.00$.
- Based on the calculated average values of dimensionality and nucleation indexes, it was concluded that the dominant crystallization mechanism is the sporadic nucleation, with a three-dimensional (3D) sphere growth of new phases.
- It was found that the contributions of the activation energies for nucleation ($E_N$) and the growth ($E_G$), to the *apparent* (*effective*) activation energy ($E_a$) of the entire decomposition process, are fractional.
- By varying the local Avrami constant with a fraction of transformation, it was found that the nucleation rate is maximal in the initial stage of the process, and then nucleation rate decreases rapidly followed by growth of the product/products particles.
- Based on the dependence of the Avrami constant ($n$) in a function of the *effective* activation energy, it was found that at $T > 950$ °C, the crystallization process take place in the autocatalytic stage, under the conditions where the rate of nucleation rapidly increases. It

was established that the high nucleation rate can be attributed to the formation of both Zn and Fe rich regions which provide a high number of heterogeneous nucleation sites, especially for the crystallization process at high operating temperatures.

- It was concluded that based on the behavior of the half-time ($t_{0.50}$) and the reciprocal half-time ($t_{0.50}^{-1}$) values with a change in the operating temperature, the highest possible crystallization rate is achieved at the highest $T$ (1,150 °C). In addition, it was also concluded that at the same operating temperature, the rate of formation of the crystal grains is the largest.
- Based on the survival analysis within the statistical interpretation of the process, it was concluded that all important products of decomposition reward after exactly 60 min from the start of monitoring the entire process.
- On the basis of the applied Weibull probability model, the corresponding density distribution function of $E_a$ values [$f(E_a)$] was derived. It has been shown that $f(E_a)$ function is positively skewed, which is characterized with a long tail on the right side, and the "*bulk*" of the $E_a$ values that lie left of the *mean* value (4.1 kJ mol$^{-1}$) (in the range of the low $E_a$ values). The resulting $f(E_a)$ function with specified characteristics is the "*fingerprint*" distribution, for the considered decomposition process.
- The proposed reactivity distribution model has proved very successful in describing the experimentally obtained kinetic (conversion) curves, for Zinc–Iron-intermetallic phase decomposition process at different operating temperatures.

**Acknowledgments** The authors would also like to thank the Ministry of Science and Environmental Protection of Serbia, under the Project 172015 (Dr Bojan Janković). We like to thank Deutsche Forschungsgemeinschaft DFG in Bonn (Germany) for financial support of the project FR 1713/13-1. Zn-recovery from steel making dusts-Kinetics and mechanism of thermal zinc-ferrite phase decomposition (Dr Srećko Stopić and Dr Bernd Friedrich).

## References

1. Stopić S, and Friedrich B, Proceeding of EMC 2009, Innsbruck, Austria (2009).
2. Polsilapa S, Sadedin D R, and Gray N B, Proceeding of EMC 2009, Innsbruck, Austria (2009).
3. Olper M, and Maccagni M, The Southern African Institute of Mining and Metallurgy, Lead and Zinc (2008).
4. Olper M, and Maccagni M, in *Fourth International Symposium on Recycling of Metals and Engineered Materials*, (eds) Stewart D L Jr., Daley J C, and Stephens R L, Pittsburgh, Pennsylvania (2000), p 379.
5. Jha M K, Kumar V, and Singh R J, *Conserv Recyc* **33** (2001) 1.
6. Havlik T, Turzakova M, Stopić S, and Friedrich B, *Hydrometall* **77** (2005) 41.
7. Kellogg H H, Rao Y K, and Marcuson S W, *Ann Rev Phys Chem* **27** (1976) 387.
8. Zhao D G, Wang S H, and Zhao P, *J Iron Steel Res* **24** (2012) 19.
9. Morcali M H, Yucel O, Aydin A, and Derin B, *J Mining Metall Sect B Metall* **48** (2012) 173.
10. Püllenberg R, *Hydrometallurgical Treatment of Zinc Concentrate Reached on Iron Afzet Partially Reduction of Roasted Residue*, Doctoral thesis, 88, RWTH Aachen University, Aachen (1981).
11. Johnson W A, and Mehl R F, *Trans Am Inst Min Metall Petrol Engin* **135** (1939) 416.
12. Avrami M, *J Chem Phys* **7** (1939) 1103.
13. Avrami M, *J Chem Phys* **8** (1940) 212.
14. Avrami M, *J Chem Phys* **9** (1941) 177.
15. Weibull W, *A Statistical Representation of Fatigue Failures in Solids*, Transactions of the Royal Institute of Technology, Stockholm (1949), p 1.
16. Weibull W, *J Appl Mech* **18** (1951) 293.
17. Murthy D N P, Xie M, and Jiang R, *Weibull Models*, Wiley, Hoboken (2004), p 3.
18. Supaphol P, and Spruiell J E, *Polymer* **42** (2001) 699.
19. Wunderlich B, *Macromolecular Physics*, vol 2, Academic Press, New York (1976), p 132.
20. Christian JW, *The Theory of Transformations in Metals and Alloys*, Pergamon Press, Oxford (1965), p 53.
21. Mittemeijer E J, *Fundamentals of Materials Science*: *The Microstructure—Property Relationship using Metals as Model Systems, Chapters 9–10*, Springer, Berlin Heidelberg (2010), p 371.
22. Friedman H, *J Polym Sci C* **6** (1964) 183.
23. Buschow K H J, *J Phys F Metal Phys* **13** (1983) 563.
24. Belfiore L A, in *Physical Properties of Macromolecules*, (ed) Belfiore L A, (1st Ed), Chapter 8, Wiley, Hoboken (2010), p 287.
25. Supaphol P, *Thermochim Acta* **370** (2001) 37.
26. Weibing X, Pingsheng H, and Dazhu C, *Europ Polym J* **39** (2003) 617.
27. Málek J, *Thermochim Acta* **200** (1992) 257.
28. Montserrat S, Málek J, and Colomer P, *Thermochim Acta* **313** (1998) 83.
29. Garitta L, and Hough G, in *Shelf Life Assessment of Food*, (ed) Nicoli M C, Chapter 7, CRC Press Taylor & Francis Group, Boca Raton (2012), p 169.
30. Klein J P, and Moeschberger M L, in *Statistics for Biology and Health*, (eds) Dietz K, Gail M, Krickeberg K, Samet J, and Tsiatis A, Chapter 2, (2nd Ed), Springer, Medford (2003), p 21.
31. Ebeling C E, *An Introduction to Reliability and Maintainability Engineering*, McGraw-Hill Companies, Inc., Boston (1997), p 23.
32. Engelhardt M, *Technomet* **17** (1975) 369.
33. Burnham A K, and Dinh L N, *J Therm Anal Calorim* **89** (2007) 479.
34. Burnham A K, and Braun R L, *Energy & Fuels* **13** (1999) 1.
35. Lakshmanan C C, and White N, *Energy & Fuels* **8** (1994) 1158.
36. Miura K, *Energy & Fuels* **9** (1995) 302.
37. Abramowitz M, and Stegun I A, *Handbook of Mathematical Functions*, NBS Applied Math. Series 55, US Department of Commerce, Washington (1964), p 257.
38. Brown M E, and Galwey A K, *Anal Chem* **61** (1989) 1136.
39. Vyazovkin S, *Int J Chem Kinet* **28** (1996) 95.
40. Vyazovkin S V, and Lesnikovich A I, *Thermochim Acta* **165** (1990) 273.
41. Cahn R W, and Haasen P, in *Physical Metallurgy*, (eds) Cahn R W, and Haasen P, North-Holland, Amsterdam-Elsevier Science B.V., Amsterdam, The Netherlands (Fourth, Revised and Enhanced Edition) (1996), p 135.

42. Hermann H, Heinemann A, Mattern N, and Wiedenmann A, *EPL (Europhys. Lett.)* **51** (2000) 127.
43. Turnbull D, *Solid State Physics*, vol 3, Academic Press, New York (1956), p 225.
44. Sangwal K, *Additives and Crystallization Processes*: *From Fundamentals to Applications*, (1st Ed), Wiley, The Atrium, Southern Gate, Chichester (2007), p 21.
45. Ding Z, and Spruiell J E, *J Polym Sci B Polym Phys* **35** (1997) 1077.
46. Offerman S E, van Dijk N H, Sietsma J, Grigull S, Lauridsen E M, Margulies L, Poulsen H F, Rekveldt M Th, and van der Zwaag S, *Science* **298** (2002) 1002.
47. Burke J, *The Kinetics of Phase Transformation in Metals*, Pergamon Press, Oxford (1965), p 191.
48. Xiaofeng W, Likai M, Wei Z, Zhongyuan S, Yi S, and Keqiang Q, *J Rare Earths* **25** (2007) 189.
49. Rosenqvist T, *Principles of Extractive Metallurgy*, (2nd Ed), Tapir Academic Press, Trondheim (2004), p 215.
50. Pineau A, Kanari N, and Gaballah I, *Thermochim Acta* **447** (2006) 89.
51. Pineau A, Kanari N, and Gaballah I, *Thermochim Acta* **456** (2007) 75.
52. Hansson R, Hayes P C, and Jak E, in VII International Conference on Molten Slags Fluxes and Salts, The South African Institute of Mining and Metallurgy, South Africa, (2004).
53. Yung S S, and Lee J S, *Mater Trans* **50** (2009) 2270.
54. Fan H J, Yang Y, and Zacharias M, *J Mater Chem* **19** (2009) 885.
55. Hagemark K I, and Toren P E, *J Electrochem Soc* **122** (1975) 992.
56. Tomlins G W, Routbort J L, and Mason T O, *J Appl Phys* **87** (2000) 117.
57. Sajadi S A A, *Am J Anal Chem* **2** (2011) 206.
58. Selim F A, Weber M H, Solodovnikov D, and Lynn K G, *Phys Rev Lett* **99** (2007) 085502.
59. Bid S, and Pradhan S K, *Mater Chem Phys* **82** (2003) 27.
60. Lawless J F, *Basic Concepts and Models*, in *Statistical Models and Methods for Lifetime Data*, (ed) Lawless J F, (2nd Ed), Wiley, Hoboken (2002), p 621.
61. Klutke G A, Kiessler P T, and Wortman M A, Reliab IEEE Trans **52** (2003) 125.